1992

Magnetically induced anisotropy and crystallization of sputter deposited cobalt-titanium binary films

Harold Jordan
San Jose State University

Order Number 1348691

Magnetically induced anisotropy and crystallization of sputter deposited cobalt-titanium binary films

Jordan, Harold, M.S.

San Jose State University, 1992

U·M·I
300 N. Zeeb Rd.
Ann Arbor, MI 48106

MAGNETICALLY INDUCED ANISOTROPY AND CRYSTALLIZATION OF SPUTTER DEPOSITED COBALT-TITANIUM BINARY FILMS

A Thesis

Presented to

The Faculty of the Department of Materials Engineering

San Jose State University

In Partial Fulfillment

of the Requirements for the Degree

Master of Science

By

Harold Jordan

May, 1992

APPROVED FOR THE DEPARTMENT OF MATERIALS ENGINEERING

4/9/92
Dr. Peter S. Gwozdz

April 9, 1992
Dr. Kiumars Parvin

April 10, 1992
Dr. Guna Selvaduray

APPROVED FOR THE UNIVERSITY

Serena M. Stanford

ABSTRACT

MAGNETICALLY INDUCED ANISOTROPY AND CRYSTALLIZATION OF SPUTTER DEPOSITED COBALT-TITANIUM BINARY FILMS

by Harold Jordan

Polycrystalline and amorphous cobalt-titanium binary films were produced using vapor deposition by simultaneous cosputtering from pure Co and Ti targets. In-plane magnetic anisotropy was induced into the film by application of an in-plane static magnetic field during sputter deposition.

Relaxation and crystallization of the metastable amorphous CoTi films were induced by heating in pure argon. The peak crystallization temperature was found to occur at 748°K, and the structures of the crystallized film products were found to be cubic $CoTi_2$ and cubic Co_3Ti.

The crystalline to amorphous structural transition was observed to occur in the titanium (solute) concentration range between 11.5 to 13.5 atomic percent titanium during sequential sputter depositions with increased Ti concentration. Bulk resistivity of the sputtered CoTi films was between 100 and 200 micro ohm-cm. Magnetically soft films with an in-plane anisotropy constant between 1 to 4.9 x 10^3 ergs/cm^3 and coercivity between 7 to 14.5 Oersteds were obtained.

TABLE OF CONTENTS

LIST OF FIGURES

LIST OF TABLES

LIST OF SYMBOLS USED

ΔG_D	Activation energy for diffusion
ΔG_{des}	Activation energy for surface desorption
ΔG_{sd}	Activation energy for surface diffusion
θ	Angle
Å	Angstrom
A	Area
k	Boltzmann constant
R_B	Bulk resistivity
$\Delta\mu$	Change in chemical potential of system
H_C	Coercivity
C_O	Composition of glass
C_{eq}	Composition of glass in equilibrium with crystal at the interface
C_Q	Composition of primary crystal
C_1	Constant
U_O	Constant
u	Crystal growth rate
E_a	Crystallization activation energy
T_C	Curie temperature
°C	Degrees Centigrade
°K	Degrees Kelvin
ΔG_V	Driving force for transformation
ΔH_{crys}	Enthalpy of crystallization
T_O	Equilibrium transformation temperature
t_f	Film thickness
ΔG	Free energy change of system
ΔG^*	Free energy of formation of critical nucleus
D_O	Grain diameter
>	Greater than
ΔH_f	Heat of transformation
J	Heterogeneous nucleation rate
K_U	Induced anisotropy constant
H_P	In-plane perpendicular anisotropy field
H_u	In-plane induced anisotropy field
γ	Interfacial surface tension
<	Less than
m	Magnetic moment
M	Magnetization

T_M	Melting point
R_C	Minimum quench rate for glass formation
$A_{\beta S}$	Nucleus-substrate area
$\gamma_{\beta S}$	Nucleus-substrate interfacial surface tension
T_X	Peak crystallization temperature
$\perp$	Perpendicular
K_P	Perpendicular (out of plane) anisotropy constant
π	Pi, 3.14159
Q	Primary crystal
r*	Radius of critical nucleus
r	Radius of nucleus
H^h_{Sat}	Saturation field in the magnetic hard direction
m_S	Saturation magnetic moment
M_S	Saturation magnetization
λ_S	Saturation magnetostriction
T_S	Substrate temperature
ΔT_S	Substrate temperature rise
T	Temperature
ΔT	Temperature change
$A_{\alpha\beta}$	Vapor-nucleus area
α	Vapor phase
P	Vapor pressure or equivalent rate of arrival
$\gamma_{\alpha S}$	Vapor-substrate interfacial surface tension
D	Volume diffusion coefficient

LIST OF ACRONYMS/ABBREVIATIONS

cm	Centimeter
Co	Cobalt
CoTi	Cobalt-titanium
Cu	Copper
$Cu_{K\alpha}$	X-ray wavelength of Copper Kα Line
DC	Direct current
DSC	Differential Scanning Calorimeter
DTA	Differential Thermal Analysis
emu	Electromagnetic unit
FCC	Face Centered Cubic
Fe	Iron
HCP	Hexagonal Close Packed
K	Potassium
KGauss	KiloGauss
Kwatt	Kilowatt
KV	Kilovolt
NBS	National Bureau of Standards
Mn	Manganese
mTorr	Millitorr
μohm·cm	Micro ohm·centimeter
Min	Minute
O	Oxygen
Oe	Oersted
RF	Radio Frequency
Sec	Second
Si	Silicon
Sm	Samarium
TEM	Transmission Electron Microscopy
Ti	Titanium
VSM	Vibrating Sample Magnetometer
XRD	X-ray diffraction
Zn	Zinc

ACKNOWLEDGEMENTS

The author wishes to express sincere gratitude for the support and services received from the following:

1. My devoted wife, Yvonne and daughter, Teresa, for numerous efforts, assistance and support during the entire preparation of the thesis material.

2. Mr. Thomas G. Beat and Mr. Jerry Beat, Delphic Thin Film Consultants, San Leandro, CA, for providing the magnetron sputtering equipment and time allocation for experimentation.

3. Dr. Peter S. Gwozdz, San Jose State University Materials Engineering Dept., for material technical review, critique and project advice.

4. Dr. Kiumars Parvin, San Jose State University Physics Dept., for material review and critique.

5. Dr. Guna Selvaduray, San Jose State University Materials Engineering Dept., for material technical review and critique.

6. Dr. David Su, San Jose State University Materials Engineering Dept., for Transmission Electron Diffraction Analysis and Transmission Electron Micrographs.

7. Mr. Boyd Taylor, Forensic Inc., Hayward, CA, for Transmission Electron Diffraction and Micrographs.

8. Mr. Dave Harris, Charles Evans Associates, Redwood City, CA, for Auger Electron Spectroscopy analysis.

9. Mr. Keith Goodson, Censtor Inc., San Jose, CA, for Vibrating Sample Magnetometer and B-H magnetic analysis.

10. Mrs. Aino Mattos and Mr. Linden Critchlow, Avantek Inc., Santa Clara, CA, for Scanning Electron Microscopy, X-ray Edax, Dektak Profilometer and Four Point Probe resistivity measurements.

11. Mr. John Rose, Rose Consulting, Half Moon Bay, CA, for Differential Scanning Calorimetry analysis.

12. Mrs. Margaret Arst and Mr. Shelesh Redkar, Signetics Inc., Sunnyvale, CA, for X-ray Diffraction analysis.

13. Mrs. Martha Pistacchi, Opticom Inc., San Jose, CA, for wordprocessing and manuscript services.

14. Mr. Floyd E Pederson, San Jose, CA, for word processing and manuscript services.

CHAPTER 1

INTRODUCTION

During the past decade, a significant amount of scientific interest has been generated in the class of materials known as amorphous metallic glasses. A very thorough compilation of data and general information concerning metallic glasses is presented by Luborsky[1] for reference.

When Shan Chan et al. have evaluated the effects of titanium concentration upon magnetic properties of bulk cobalt-titanium alloys.[2] Sputter deposited films of crystalline and amorphous cobalt-titanium have also received attention by several researchers[3,4,5] and is the subject of this investigation. The effects of adding titanium (solute) to pure cobalt (solvent) to form cobalt-titanium thin films by radio frequency (RF) sputtering was presented in one of the earliest investigations of cobalt-titanium films by J.A. Aboat and E. Klokhom.[6] They evaluated the effects of titanium concentration upon properties such as resistivity and saturation magnetostriction, λ_S. The effects of titanium concentration upon other properties such as saturation magnetization, M_S, and Curie temperature, T_C, for sputtered cobalt-titanium films were subsequently evaluated by G. Suran et al.[7]

When titanium was added to pure cobalt in successive increments by RF sputtering, a distinct discontinuity in both the bulk film resistivity, R_B, and

saturation magnetostriction, λ_S, was found to exist at the crystalline to amorphous structural transformation which occurred at approximately 14 atomic percent titanium concentration in the film. Below 14 atomic percent titanium, the cobalt-titanium film manifested a crystalline structure, and for titanium concentration above 14 atomic percent, the film exhibited an amorphous structure.

The magnetic and structural properties of amorphous CoTi films were recently evaluated by G. Suran and others[8,9,10,11,12] who observed two uniaxial anisotropy fields, H_p and H_u, corresponding to perpendicular and in-plane anisotropies, respectively, when the films were RF sputtered in the presence of an in-plane applied magnetic field. Soft magnetic films were produced with small coercivity, H_C. In-plane magnetic anisotropy was induced into the CoTi film in the direction of the applied magnetic field during sputter deposition. The magnetic and structural properties of soft amorphous CoTi films were extremely sensitive to the deposition temperature, T_S, of the substrate. The formation of perpendicular anisotropy, H_p, was also related to the substrate temperature.

However, RF sputtering of many materials at typical target-to-substrate spacings of 1 to 2 inches can produce significant substrate heating during sputter deposition. Due to the extreme sensitivity of the CoTi film properties to the substrate temperature, the need to produce these films with minimized

substrate heating clearly exists.

Crystallization studies of amorphous $Co_{78}Ti_{22}$ ribbons were recently conducted.[13] The crystallization behavior was evaluated using Differential Thermal Analysis (DTA). The crystallization sequence at a heating rate of 8.33 x $10^{(-2)}$ °K/sec began by the sequential formation of two metastable FCC phases, Co_2Ti and Co_3Ti, which crystallized at 777 °K and 823 °K, respectively. The crystallization sequence proceeded from an amorphous to metastable crystalline structure initially upon heating. Subsequent heating for longer time produced a mixture of Co_3Ti and Co_2Ti phases.[14] The amorphous range for cobalt-titanium ribbon was also noted to lie close to the deep eutectic region of the CoTi equilibrium phase diagram.[15]

The nature of the crystallization path of sputter-deposited amorphous cobalt-titanium films during heat treatment in pure argon was evaluated in this thesis investigation. The structures of the crystallized film products were determined. Such information related to the thermal stability of these films was not found published for sputtered CoTi and the need for such evaluation was clearly warranted. The cobalt-titanium films were sputtered using DC Magnetron cosputter with large target-to-substrate spacing to minimize the substrate temperature during the deposition. The effect of minimized substrate temperature was to increase the amount of undercooling below an equilibrium transformation temperature. The deposition was performed with the substrate

located inside an in-plane applied magnetic field. Previously reported publications were concerned with cobalt-titanium films deposited with RF power with small target-to-substrate spacing. The influence of such differences in sputter deposition techniques upon cobalt-titanium film properties was not found in the literature and was also evaluated in this investigation.

A summary of the theoretical aspects of the thermodynamics and kinetics of metallic glass formation and crystallization is presented in Chapter Two along with relevant theories of ferromagnetism. The summary was prepared from published literature. Chapter Three describes the experimental apparatus and procedures used in the experimentation along with measurements and accuracies. Experimental data and results are given in Chapter Four. A summary of results and discussion are presented in Chapter Five. Chapter Six presents the conclusions from the investigation with recommendations for further investigation.

CHAPTER 2

THEORETICAL CONSIDERATIONS

Theoretical Perspective

Glass formation by vapor quenching requires that a change of state from the vapor state to the solid state is made by the quenched species. The glass formed exists in a metastable equilibrium state which is different from the most stable thermodynamic equilibrium state. The description of glass formation involves the discussion of the thermodynamic and kinetic factors which permit the probability of formation of a metastable phase by the quenched species instead of the most stable-equilibrium phase during the vapor-solid phase transformation.

The requirement for glass formation upon solidification is that the quenching rate must be such that crystallization is avoided. Crystallization involves the process of nucleation. The formation of the metastable glass requires the avoidance of the formation of crystalline nuclei and their subsequent growth. The formation of amorphous CoTi films by sputter deposition in this thesis investigation is described by discussing the thermodynamic and kinetic factors which influence the thermodynamic stability and the rate of nucleation and growth of the solid nuclei formed upon solidification from the vapor state. Glass formation is promoted by those

conditions which suppress the nucleation and growth of the most stable equilibrium phase upon solidification. Crystallization of amorphous CoTi upon heating in argon is treated as homogeneous nucleation within the amorphous solid matrix, and can be treated as a solid-solid phase transformation.

Theoretical models which explain the occurrence of ferromagnetism and induced magnetic anisotropy in polycrystalline and amorphous materials are discussed. The implications from these models are discussed where applicable to the results obtained from this investigation.

Thermodynamics and Kinetics of Glass Formation and Crystallization

Phase Transformation and Glass Formation

For a spontaneous transformation of a system to occur from the vapor state 1 to the solid state 2, the necessary condition for the transformation is given by,[16,17,18]

$$\Delta G = G_2 - G_1 < 0 \qquad (1)$$

where ΔG = Gibbs free energy change of the system,

G_2 = Gibbs free energy of the final solid state,

G_1 = Gibbs free energy of the initial vapor state.

The transformation does not necessarily proceed directly to the stable equilibrium state of lowest free energy, but can pass through a series of intermediate metastable states which exist at a local minimum in the Gibbs free energy. The metastable equilibrium state, B, shown in Figure 1 is distinguished from the stable equilibrium state, A, because the metastable state does not possess the lowest Gibbs free energy.

The general theory of glass formation by liquid-solid and vapor-solid transformations has been presented by D.R. Uhlmann and H. Yannon[19], H.A. Davies[20] and P.F. James[21]. The essential requirement for amorphization of solids quenched from the liquid or vapor state is that the cooling rate must exceed a minimum cooling rate, R_C, such that no observable crystallization occurs during quenching.

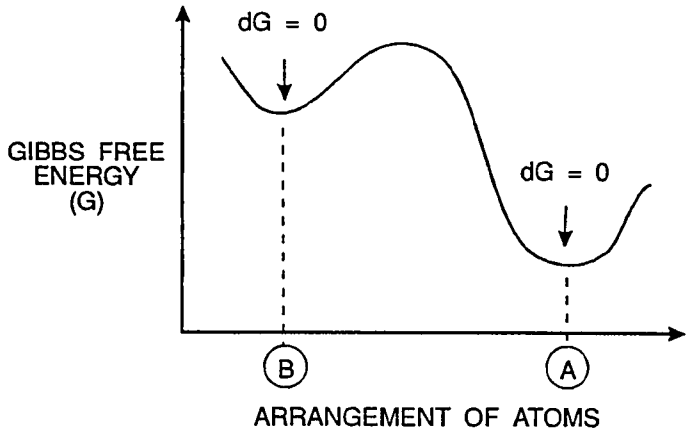

Figure 1. Gibbs free energy variation with the arrangement of atoms. (A) = stable equilibrium, lowest free energy. B = metastable equilibrium, higher free energy.

Solidification from the Vapor State

Solidification of Co and Ti vapor species by sputtering requires direct transformation from the vapor state to the solid state. Nucleation of vapor species upon a solid substrate is described as heterogeneous nucleation. The theory of condensation from the vapor state has been presented by J.P. Hirth[22] and J.P. Hirth and G.M. Pound[23]. Subsequent treatments have been presented by J.W. Christian,[24] B.L. Lewis and J.C. Anderson,[25] M.G. Scott and R. Maddin[26] and A.R. Adamson.[27] Heterogeneous nucleation of a spherical nucleus is shown in Figure 2[28] and Figure 3[29]. Figure 2 and Figure 3 illustrate the geometrical parameters and the surface interactions between the deposited nucleus, the vapor phase and the substrate. The mechanism of

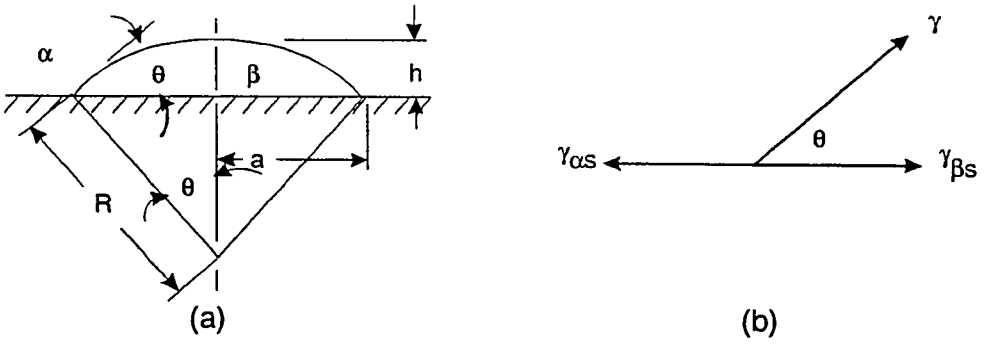

Figure 2. Heterogeneous nucleation parameters.

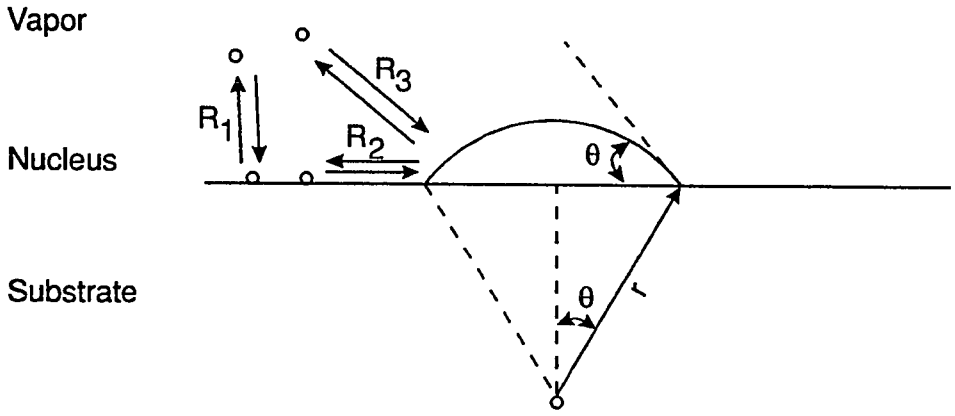

Figure 3. Cross section of spherical cap-shaped nucleus on substrate.

growth of the nucleus by addition of adatoms directly from the vapor state and by surface diffusion is illustrated in Figure 3.

For heterogeneous nucleation in a one-component system, the change in free energy upon formation of an embryo is given by, [30]

$$\Delta G = \frac{4}{3}\pi r^3 \Delta G_V + A_{\beta S}(\gamma_{\beta S} - \gamma_{\alpha S}) + A_{\alpha\beta}\gamma \qquad (2)$$

where $A_{\beta S}$ = Area of the interface shared by the deposited nucleus and the substrate,

$A_{\alpha\beta}$ = Area of the interface shared by the deposited nucleus and the vapor phase,

$\gamma_{\beta S}$ = deposited nucleus - substrate interfacial surface tension

$\gamma_{\alpha S}$ = vapor phase - substrate interfacial surface tension and

γ = vapor phase - deposited nucleus interfacial surface tension.

Using the Young Equation,

$$\gamma_{\beta S} - \gamma_{\alpha S} = -\gamma \cos\theta \qquad (3)$$

the critical radius for nucleation was determined[31] by maximizing,

$$\frac{\partial \Delta G}{\partial r} = 0 \qquad (4)$$

and the critical radius shown in Figure 4[32] is given by,

$$r^* = \frac{-2\gamma}{\Delta G_V} \qquad (5)$$

The free energy barrier to the formation of the critical nucleus having a radius of r* is given by,

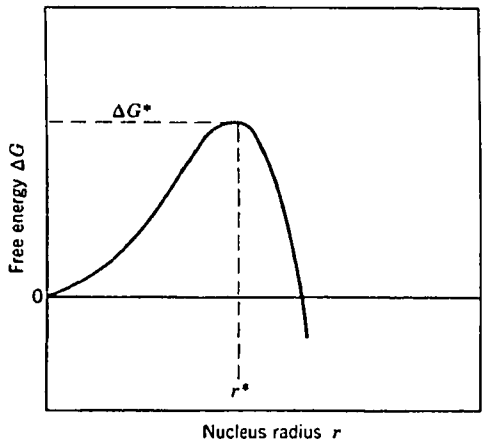

Figure 4. Nucleation and growth process

$$\Delta G(r*) = \Delta G* = \frac{-16\pi\gamma^3}{3(\Delta G_V)^2} \cdot f(\theta) \tag{6}$$

where

$$f(\theta) = \frac{(2 + \cos\theta)(1 - \cos\theta)^2}{4} \tag{7}$$

Figure 4 shows that the free energy of the system, ΔG, can be reduced by growth of nuclei of size greater than r* or by creation of smaller nuclei with size less than r*. The heterogeneous nucleation rate is given by,[33,34,35]

$$J = C_1 \cdot p \cdot \exp\left(\frac{\Delta G_{des}}{kT}\right) \exp\left[\frac{-(\Delta G_{Sd} + \Delta G*)}{kT}\right] \tag{8}$$

where p = vapor pressure or the corresponding rate of arrival of incident atoms,

ΔG_{des} = activation energy for desorption from the surface,

ΔG_{Sd} = activation energy for a surface diffusion jump,

ΔG^* = free energy barrier to the formation of a stable nucleus,

T = substrate temperature.

C_1 = constant over a range of p and T.

Formation of metastable amorphous glass is favored under conditions where the heterogeneous nucleation rate of stable crystal nuclei diminishes. In the nucleation and growth process, ΔG_{des}, the activation energy for desorption from the surface, must be large enough such that a significant number of deposited atoms stick to the substrate surface. For a constant deposition rate, the heterogeneous nucleation rate of stable nuclei is influenced by the values of substrate temperature, T, the activation energy for surface diffusion, ΔG_{Sd}, ΔG_{des} and ΔG^*.

Effects of Low Substrate Temperature

The effects of substrate temperature upon heterogeneous nucleation rate were described qualitatively using an approximation to the free energy change upon crystallization by C.V. Thompson and F. Spaepen,[36,37]

$$\Delta G_V = \Delta H_f\left(1 - \frac{T}{T_o}\right) = \frac{\Delta H_f \, \Delta T}{T_o} \qquad (9)$$

where ΔH_f = enthalpy of transformation,

T_o = equilibrium transformation temperature,

ΔT = extent of undercooling, $T_o - T$.

At large undercooling, ΔT, the driving force for the transformation, ΔG_v, increases. Because r* and ΔG^* are both inversely related to ΔG_v, both r* and ΔG^* decrease at low substrate temperature. At low substrate temperature, T, the activation energy for surface diffusion, ΔG_{Sd} becomes greater than ΔG^*, and the ΔG_{Sd} term in equation (8) for the heterogeneous nucleation rate becomes dominant. Consequently, the nucleation rate becomes reduced by limited surface diffusion of deposited species. At low substrate temperature, where the surface mobility is low, the structure of the deposited film favors short-range order such as the metastable amorphous structure.[38] Glass formation by vapor-solid transformation processes requires quench rates of approximately 10^{13} °K/second, while glasses quenched from the liquid state are typically quenched at 10^6 °K/second.[39]

In the case where the vapor consists of binary species, the expressions for r* and ΔG^* are given by,[40,41,42]

$$r^* = \frac{2\gamma}{\Delta\mu_V} \tag{10}$$

and

$$\Delta G^* = \frac{-16\pi\gamma^3}{3(\Delta\mu_V)^2} \cdot f(\theta) \tag{11}$$

respectively, where the driving force for the vapor-solid transformation is represented by $\Delta\mu_v$, the change in chemical potential of the system. At low

substrate temperature (300°K or less), $\Delta\mu_v$ becomes large, while r* and ΔG^* both become small. The activation energies for surface diffusion for both binary species becomes large and the formation of a binary-metastable amorphous phase occurs at low substrate temperature.

Crystallization of Metallic Glasses

The general theory of crystallization of glasses has been presented by J.W. Mullin[43], C.G. Bergeron[44] and R. Elliott[45]. Most metallic glasses crystallize upon heating by eutectic crystallization or primary crystallization.[46,47] During eutectic crystallization, devitrification occurs by homogeneous nucleation and growth of crystals within the amorphous matrix.[1]

In metallic glasses which crystallize by eutectic crystallization, the growth rate has been shown to follow an Arrhenius relationship at large undercooling and is given by,[48,49]

$$u = u_o \exp\left(\frac{-\Delta G_D}{kT}\right) \qquad (12)$$

---

[1]Eutectic crystallization of an amorphous matrix occurs by nucleation and growth within the matrix of two-phase barrel-shaped crystals. Each crystal contains two finely-spaced crystalline phases. The overall composition of the crystal and the amorphous matrix remain the same.

Primary crystallization occurs by nucleation and growth of crystals with composition which is different from that of the amorphous matrix. The primary phase may be either a terminal solid solution or an intermediate phase. The morphology of the primary crystals can range from spherical to highly dendritic.

where u_o = a pre-exponential factor on the order of 10^3 m/s,

ΔG_D = activation energy for an atom to leave the matrix and attach itself to the growing phase.

During primary crystallization, crystals of various shapes may be produced. A free energy vs. composition diagram for primary crystallization is shown in Figure 5.[50] The diagram shows that the overall free energy, G, of the metastable amorphous glass is reduced to a point on the common tangent line by nucleation and growth of the primary phase which is represented by Q. The radial growth rate for spherical nuclei has been found to follow a parabolic relationship with anneal time and is given by,[51]

$$r = b\sqrt{Dt} \tag{13}$$

where D = the volume diffusion coefficient,

b = a dimensionless parameter evaluated from the composition at the particle interface and the composition of the sample.

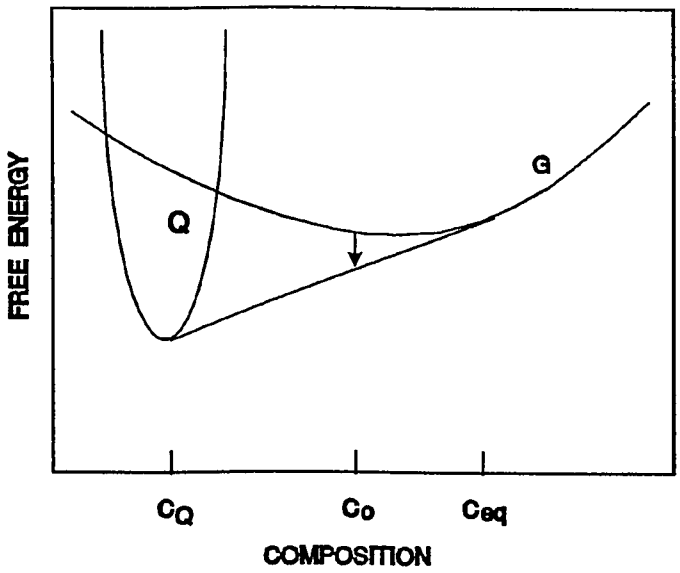

Figure 5. Free energy diagram

C_o = composition of the glass

C_Q = composition of the crystal

C_{eq} = composition of glass in equilibrium with crystal at the interface

Polycrystalline and Amorphous Ferromagnetism

Induced Magnetic Anisotropy

The crystal anisotropy forces which bind the spontaneous magnetization, M_S, of any domain to an easy direction can be expressed in an indirect manner.[52] The anisotropy field, H_u, is a fictitious field which is parallel to the easy direction in a material. For a uniaxial crystal, the anisotropy field is the field which can completely overcome the anisotropy forces when applied 90° to the easy axis by rotating M_S through 90°.[53] For a uniaxial crystal, the anisotropy field is given by,[54,55]

$$H_u = \frac{2K_u}{M_s} \tag{14}$$

where M_S = saturation magnetization and,

K_u = anisotropy constant.

Polycrystalline Ferromagnetism

In a polycrystalline material, individual grains are randomly oriented. Any magnetic anisotropy of individual grains will average out and the material as a whole will exhibit no crystal anisotropy. When the crystals have a preferred orientation (texture), the polycrystalline aggregate will have an anisotropy determined by that of individual crystals.[56] By applying a magnetic field in a specific direction during pressing and sintering a powder, an easy axis

orientation can be induced into polycrystalline materials.[57]

Theoretical models have been proposed for ferromagnetism in polycrystalline materials such as that of Globus where a spherical grain is divided into two 180° magnetic domains by a domain wall, as shown in Figure 6.[58,59] Magnetic domains are pinned to the boundaries of grains in close proximity and undergo a bowing action in an applied magnetic field. The close proximity of the grains allows a strong magnetic coupling between grains and the polycrystalline material exhibits magnetism in the presence of an applied magnetic field. For non-spherical elongated grains, the Chain of Spheres model of ferromagnetism has been proposed where the magnetism is related to the contact area between spherical segments of elongated grains.[60,61]

Field induced magnetic anisotropy, K_u, in polycrystalline materials has been explained by directional atomic-pair ordering in crystalline alloys.[62] In the presence of an external applied magnetic field, atomic pairs tend to align in a direction which minimizes the total magnetic energy of the material. The alignment occurs by relative motion of the two atoms via diffusion. The material consequently exhibits a uniaxial magnetic anisotropy.

Amorphous Ferromagnetism

Ferromagnetism in amorphous alloys has been reported for several metallurgical systems. The magnetic properties of ferromagnetic amorphous

alloys have been explained by E.P. Wohlfarth using an itinerant electron model of ferromagnetism.[63] Electrons responsible for ferromagnetism in this model are considered non-localized and are capable of motion from one atom to another. Induced magnetic anisotropy in amorphous materials has also been explained using directional order theory.[64,65] However, the corresponding directionality in the amorphous material occurs by short range diffusion. The directionality exists in the form of a local collective-atomic arrangement of atoms rather than by pair-ordering as proposed for crystalline materials.

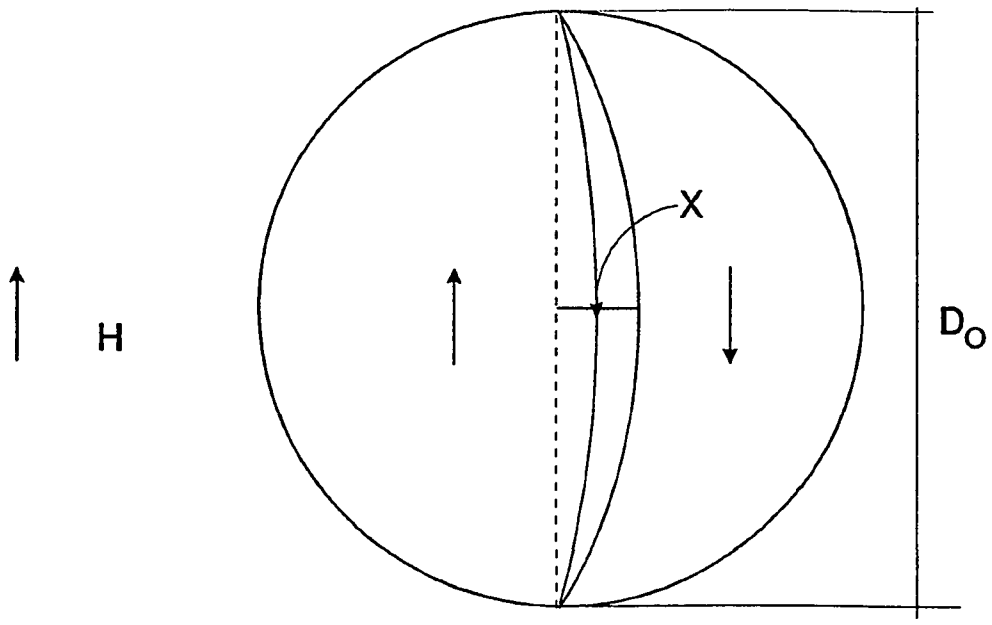

Figure 6. Domain wall bowing for an applied field H in Globus model.

CHAPTER 3

EXPERIMENTAL PROCEDURES

Experimental Set-up

The experimental set-up for cosputter deposition of cobalt-titanium inside an in-plane magnetic field included a substrate holder assembly which is shown schematically in Figure 7. The actual substrate holder assembly is shown in Figure 8. The substrate holder was a small rectangular box made from pure copper material. A water cooling jacket was located inside the copper substrate holder for water cooling capability. The top surface of the copper holder was stamped with six 0.75" x 0.75" indentations for substrate placement during deposition.

The substrate holder was located between two SmFeCo rectangular magnet bars which were 1.8" x 0.75" x 0.6" in dimensions. The permanent magnets were magnetically held onto the surface of a U-shaped plate made from plain carbon steel material which was 6.5" long x 0.125" thick. The plain carbon steel contained 98.0% Fe, 1.25% Mn and less than 1.0 weight-percent carbon. The gap spacing between the magnets was fixed at 1.70 inches. The U-shaped plain carbon steel plate was bolted to the bottom of the vacuum chamber and held in place.

An aluminum mask plate which contained a 1.25" x 1.25" square

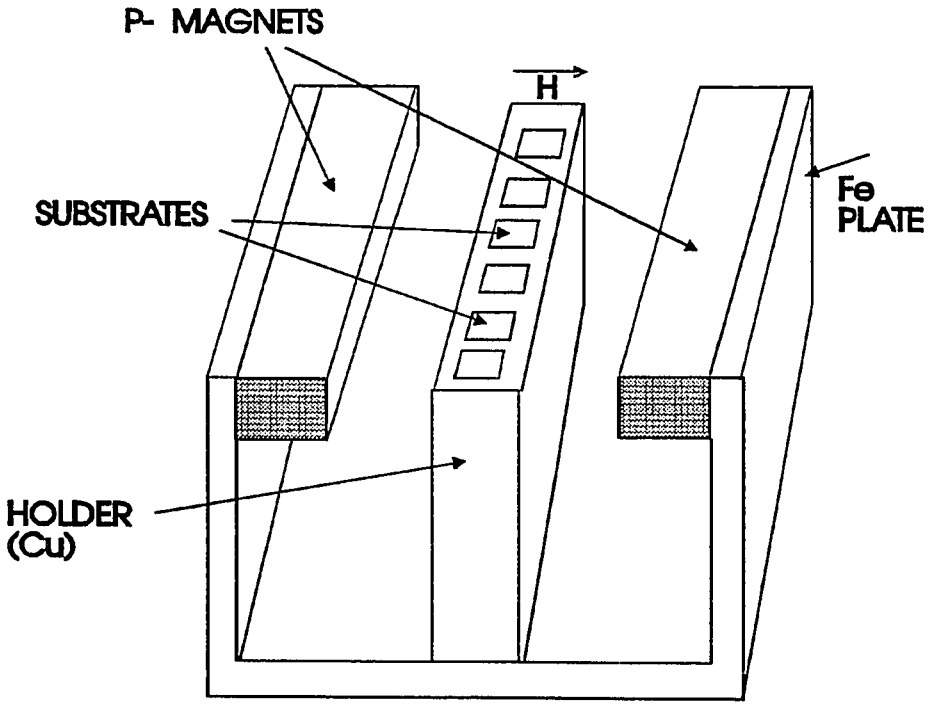

Figure 7. Substrate holder, permanent magnet assembly

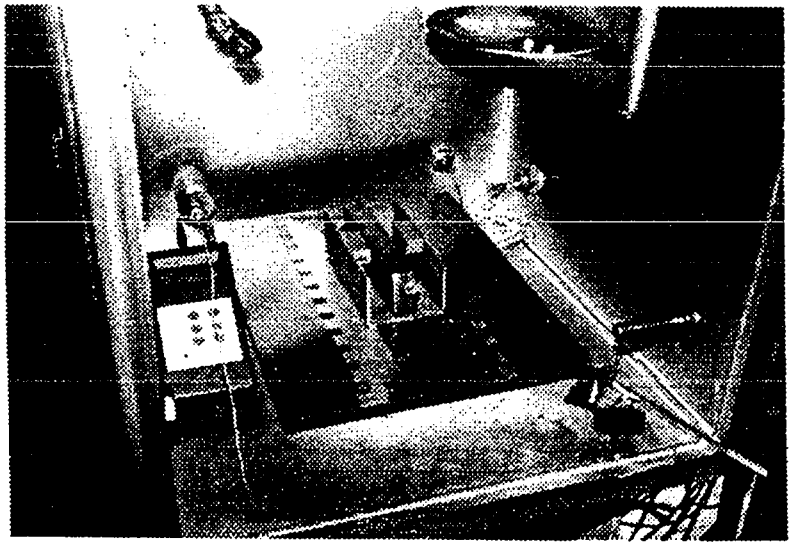

Figure 8. Magnet assembly with substrate holder and substrates

aperture was located above the substrate holder. The cobalt-titanium metal was sputtered through the aperture onto individual glass slides which were 0.75" x 0.75" x 0.10" in dimensions. A wire was connected to the shaft of a mechanical rotary feedthrough in the vacuum chamber which housed the substrate assembly. The rotary feedthrough could be turned to move each substrate under the aperture into the deposition position. The mask plate and feedthrough shaft are shown in Figure 9. A movable shutter was situated between the sputtering targets and the substrates and is shown in Figure 10.

The sputtering targets are shown in Figure 11. The cobalt target was six inches in diameter and was located 15.0" directly above the substrates. The Ti target was 2.0" in diameter and was located 8.0 inches from the center of the cobalt target. The sputter targets and substrate holder assembly were located inside a Box Sputter System for sputter deposition.

Apparatus

The Delphic Box Sputter apparatus with associated electronics is shown in Figure 12. The internal vacuum chamber was pumped by a Welch Duo-Seal mechanical pump and an APD Cryogenics 6-inch cryopump. A vacuum feedthrough allowed placement of a chromel-alumel thermocouple on the surface of the aluminum mask plate for substrate temperature measurement with a Doric Digital temperature readout. The vacuum chamber was isolated

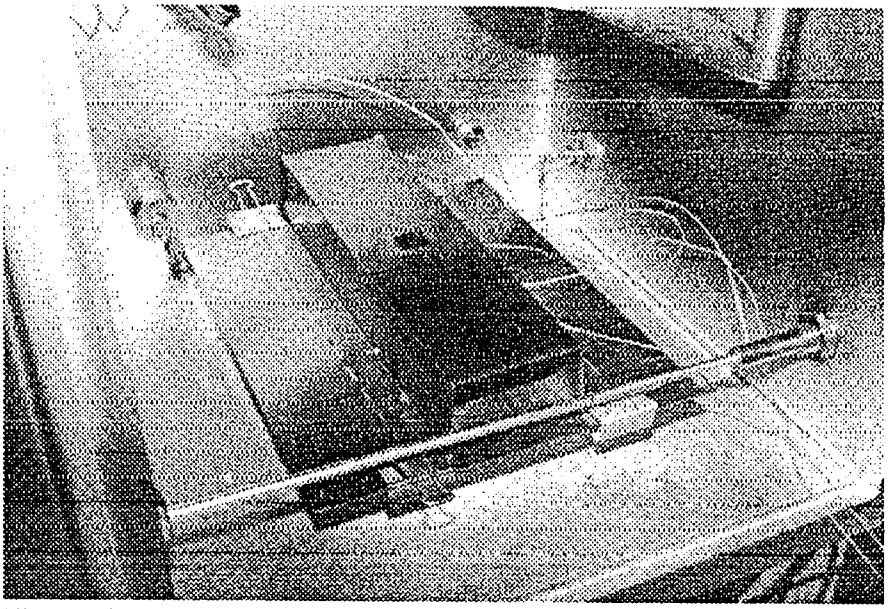

Figure 9. Rotary feed-through rod which pulls substrates

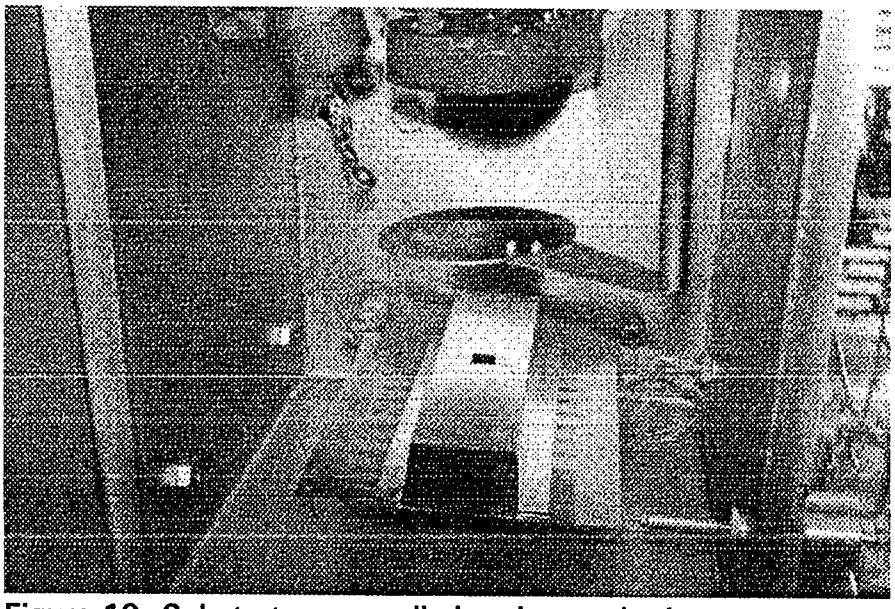

Figure 10. Substrates are pulled under mask plate

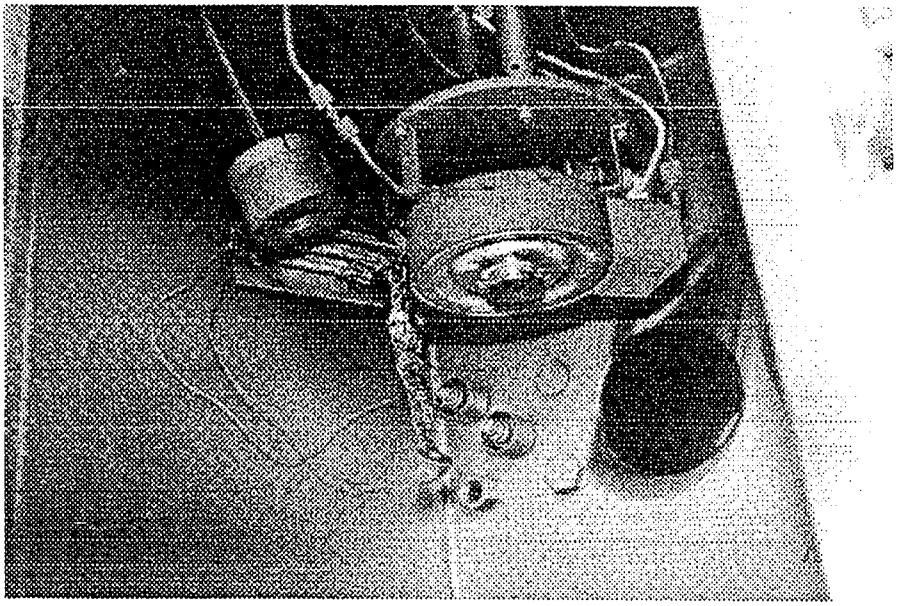

Figure 11. Cobalt and titanium targets

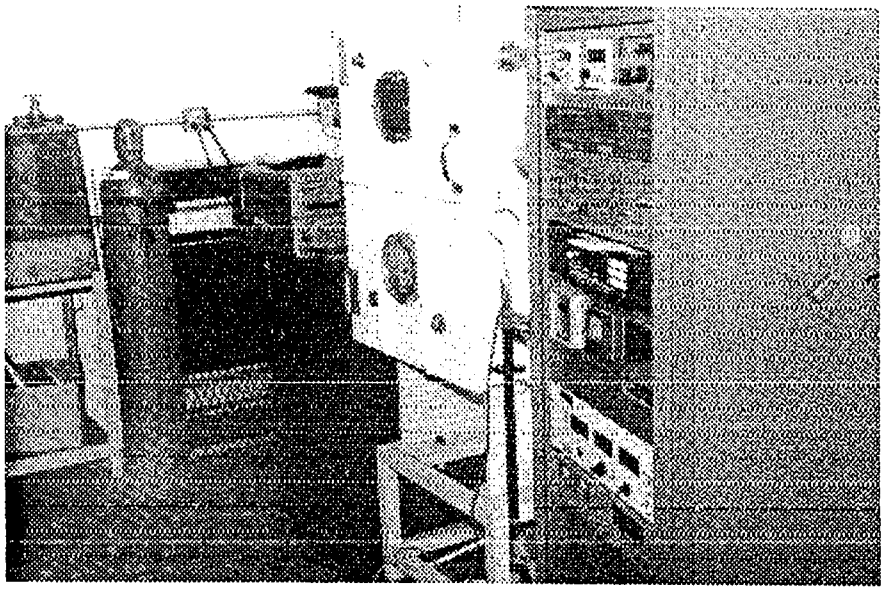

Figure 12. Delphic Box Sputter (center)

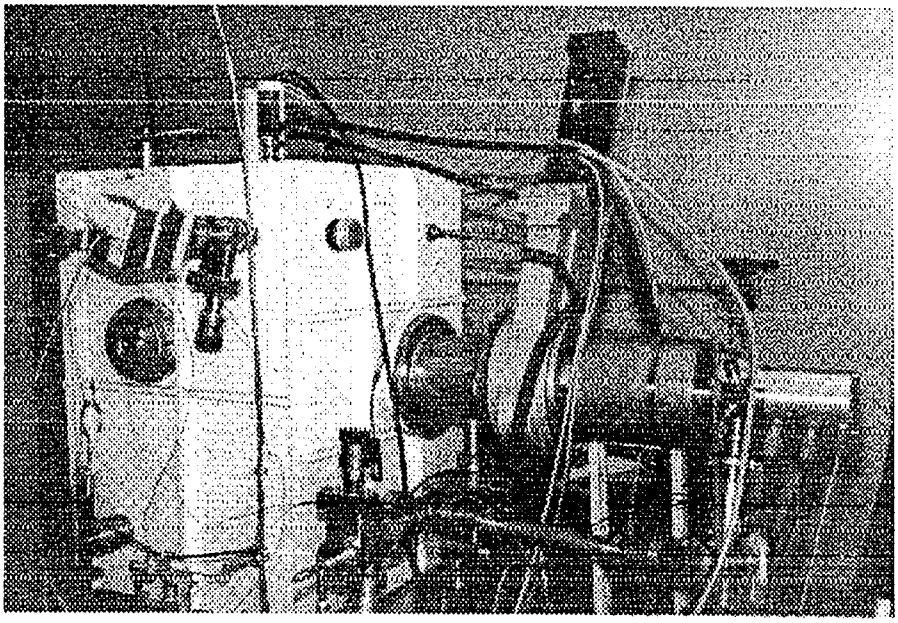

Figure 13. Box sputter and pneumatically operated gate valve

from the pumping arrangement through a pneumatically operated gate valve shown in Figure 13. The cobalt target was powered by an Eratron 1KV-10 Kwatt DC power supply and the titanium target was powered by an Allen Jones 100 volt DC power supply. Both targets were water cooled with chilled water at a 10-gallon per minute flow rate. The argon sputter gas was electronic grade 99.999 percent pure argon.

Methodology

Sample Preparation

The substrates were 0.75" x 0.75" x 0.010" glass slides. The elemental constituents in the glass were determined by x-ray spectroscopy and are shown in the Appendix. The glass substrates were cleaned in industrial grade isopropyl alcohol and blown dry with filtered nitrogen before loading into the sputter chamber. The substrates were baked at 100 °C for a minimum of 18 hours in-situ under vacuum at 2×10^{-6} Torr pressure and allowed to cool to room temperature before the deposition began in order to remove any residual volatile contaminants from the substrate surface and thus enhance film adhesion to the substrate surface.

The glass substrate with a one-micron thick amorphous $Co_{86.5}Ti_{13.5}$ film was scribed into several small sections and placed into a platinum cup used for Differential Scanning Calorimetry analysis. The $Co_{86.5}Ti_{13.5}$ film was heated at a constant heating rate of 20 °C/min in the Perkin Elmer DSC-2 Differential Scanning Calorimeter in a pure argon environment to a temperature of 525 °C.

The scribed sections of glass plus $Co_{86.5}Ti_{13.5}$ which were heated to 525 °C in argon in the DSC were subsequently mounted onto a similar glass slide and held in place by a thin gel layer. The slide was used for X-ray diffraction analysis of the crystallized CoTi structure.

Sputter Deposition Procedure

The substrate holder could hold six substrates and each substrate could be deposited as a single deposition run during a single vacuum pump-down. The depositions were performed in a fixed magnetic field of 1.3 K Gauss in the substrate plane.

The vacuum chamber was presputtered with pure titanium with closed shutter for 15 minutes at the beginning of each deposition sequence. The titanium acted as a gettering agent for any residual oxygen in the vacuum environment to minimize the oxygen content in the sputtered CoTi alloy. This was followed by a 10-minute presputter using both cobalt and titanium targets prior to deposition. The deposition pressure was 2.0 mTorr. The deposition began and ended by opening and closing the shutter, respectively. The deposition power, sputtering pressure and substrate temperature were monitored throughout the deposition process. The deposition rate and the concentration of the CoTi alloys were varied by changing the cobalt sputter power while maintaining a constant titanium sputter power at 60 watts.

Measurements - Accuracies

Substrate Temperature (°C)

The substrate temperature was measured during sputter deposition using a chromel-alumel Type K thermocouple attached to the surface of the metal mask plate approximately 1/4" from the actual substrate. Temperature was displayed on a Doric Trendicator #400A Digital Readout. For calibration purposes, temperature was measured with the thermocouple at the melting point of ice (0°C) and at the melting point of pure gallium (29.8°C) with a measurement accuracy of ±0.7 °C.

Base Vacuum Pressure (Torr)

The chamber base vacuum pressure of the Box Sputter System was measured using a Phillips Ion Gauge with a Granville-Phillips Ion Gauge Controller #280. Measurement accuracy was estimated at ±10% of the measured pressure (Torr) with a fully degassed ion gauge.

Sputter Deposition Pressure (mTorr)

The sputter deposition pressure was measured using a Vacuum General #80-6B Capacitance Manometer. The measurement accuracy was ±10% of the measured pressure (mTorr).

Sputter Deposition Time (Seconds)

Deposition time was measured with a stopwatch with 1.0 second time intervals. Measurement accuracy was ±1.0 second.

Applied Magnetic Field (Gauss)

The in-plane applied magnetic field was measured using a F.W. Bell No. 4048 Gauss-Tesla fluxmeter. The magnetic flux was measured at 1.3 KGauss ±5% over the substrate deposition area. The measurement accuracy was ±10% of the measured flux (KGauss).

Sputter Deposition Power (Watts)

The cobalt deposition power was measured using an Eratron Digital Power Supply readout. Measurement accuracy was ± 10% of displayed power (watts).

The titanium deposition power was measured using separate DC Current (I) and Voltage (V) meters with power (watts) as (I x V) ±20%.

Film Thickness (Angstroms)

The sputtered film thickness was measured over a step created in the deposited film during deposition by placing a small glass chip on the sample before deposition as a mask to the deposit. The thickness of the film step was

measured using a Dektak Profilometer. The measurement accuracy of the profilometer was checked prior to film thickness measurement using an NBS traceable standard step gauge. The film thickness (angstroms) accuracy was ±5% of the measured value.

Film Sheet Resistivity (Ohms per Square)

The sheet resistivity of the sputtered film was measured with an Avantek in-house Four Point V/I Probe meter. The probe accuracy was checked prior to film resistivity measurement using an NBS traceable resistivity standard. The measurement accuracy was ±5% of the measured value.

Bulk Film Resistivity (Ohm·Cm)

The bulk film resistivity was calculated from the film thickness and sheet resistivity by

$$R_B = R_S \cdot t_f \ (ohm \cdot cm) \qquad (15)$$

where R_S = sheet resistivity (ohms/square) and

t_f = film thickness (cm)

Accuracy was estimated as ±10% of the calculated value.

Sputtered Film Composition

The cobalt-titanium film composition was measured with a Charles Evans Auger Electron Spectrometer. The measured accuracy was estimated as ±5 atomic percent.

Peak Crystallization Temperature (0°C)

The peak crystallization temperature of the amorphous CoTi film was measured with a Perkin Elmer DSC-2 Differential Scanning Calorimeter. For calibration purposes, the DSC temperature was measured at the melting point of a zinc standard (419.5°C) before the crystallization temperature of CoTi was measured. The measurement accuracy was ±2.0°C from the measured temperature.

CoTi Crystallized Structure

The crystallized structure of the heated CoTi film was determined with a Phillips X-ray Diffractometer using $Cu_{K\alpha}$ radiation with $\lambda = 1.542$ Å. The 2θ angular measurement accuracy was ±0.1 degree. The crystal structure d-spacing accuracy was ±0.05 angstroms.

CoTi Polycrystalline Preferred Orientation

The polycrystalline preferred orientation was determined from the

Transmission Electron Diffraction patterns taken on a Phillips Model 500 Transmission Electron Microscope. The measurement accuracy of d-spacings obtained from the diffraction patterns was ±0.1 angstrom.

Magnetic Moment vs. H Field

The m (emu) vs. H (Oe) curves were obtained using an EG and G Princeton #155 Vibrating Sample Magnetometer. The saturation magnetization, M_S, was calculated by,

$$M_S \left(\frac{emu}{cm^3}\right) = \frac{m_S\ (emu)}{volume\ of\ film\ (cm)^3} \qquad (16)$$

where m_S = saturation magnetic moment.

The accuracy of the VSM was verified using a pure Nickel NBS traceable standard with magnetic moment of 5.06 emu ±5%. Calibration readings were 5.06 ±0.02 emu. The volume of film was calculated by, volume = sample length x sample width x film thickness for a rectangular sample. Length and width were measured with a micrometer (mils). All dimensions were converted to cm (1.0 inch = 2.54 cm). Accuracy was estimated as ±10% of the calulated value. Magnetic moment (m) vs. H hysteresis loops were obtained in the sample in-plane easy axis direction and the perpendicular (out of plane) hard direction.

Magnetic Coercivity (Oe)

The film coercivity, H_C, was measured using a Censtor in-house B-H Looper. The coercivity accuracy was checked by running a current (I) vs. H (Oe) curve. The H field was checked using a Hall probe and Gauss meter. The H field accuracy was ±10% of the measured value.

Anisotropy Field H_u (Oe)

The anisotropy field was measured along the sample in-plane hard direction using the B-H Looper. The value of H_u was measured as the H field at initial saturation. Accuracy was estimated as ±10% of the measured value.

Anisotropy Constant K_u(ergs/cm^3)

Anisotropy constant was calculated by

$$K_u\left(\frac{ergs}{cm^3}\right) = \frac{H_u\ (Oe)\ x\ M_S\left(\frac{emu}{cm^3}\right)}{2} \qquad (17)$$

Accuracy of measurement was estimated as ±20% of the calculated value. This calculation was made as an approximation of the in-plane anisotropy constant, K_u, with the assumption that the perpendicular (out of plane) anisotropy constant, K_P, was negligible.

CHAPTER 4

EXPERIMENTAL RESULTS

Sputter Deposition Parameters and Film Properties

Deposition Rate

The deposition rate during cosputter deposition was calculated as the ratio of film thickness/deposition time. A plot of the measured deposition rates of CoTi films as a function of Co deposition power is shown in Figure 14. The deposition rate varied from 5 Å/min to 70 Å/min. The deposition rate varied linearly with the cobalt sputter power.

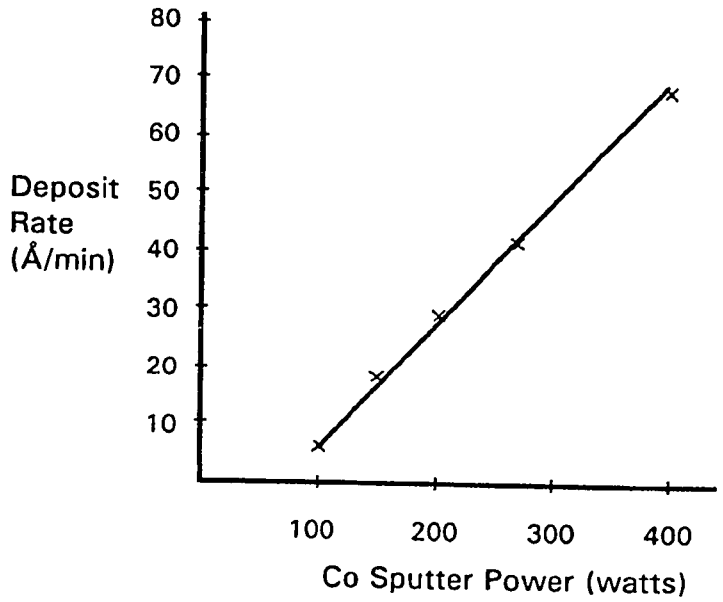

Figure 14. CoTi film deposition rate vs. cobalt sputter power

Substrate Temperature

The temperature, T_s, of the substrate during cosputter deposition was measured by a thermocouple connected to the fixed aluminum mask plate containing the deposition aperture through which CoTi films were sputtered. The measured temperature rise of the substrate above room temperature during sputter deposition of the polycrystalline CoTi films is shown in Figure 15 along with the temperature rise of the substrate during sputter deposition of an amorphous $Co_{86.5}Ti_{13.5}$ film sputtered at 150 watts Co power. It was noted that the temperature rise during sputtering increased proportionally to the Co sputter power and remained close (0-1°C) to room temperature for the amorphous CoTi films while the temperature rise for the polycrystalline films varied (3-5°C) over a wider temperature range.

Cobalt-Titanium Film Composition

The concentration of Ti in the cosputtered CoTi films was measured by Auger Electron Spectroscopy and is shown as a function of Co sputter power in Figure 16. Auger depth profiles of CoTi films deposited at several Co power levels are shown in Figure 17, Figure 18 and Figure 19. The profiles showed a low level of residual oxygen (< 5 atomic percent) present in the films. The Ti concentration varied from 7 atomic percent to 20 atomic percent as the cobalt sputter power was varied from 400 watts to 100 watts. Plots of R_B

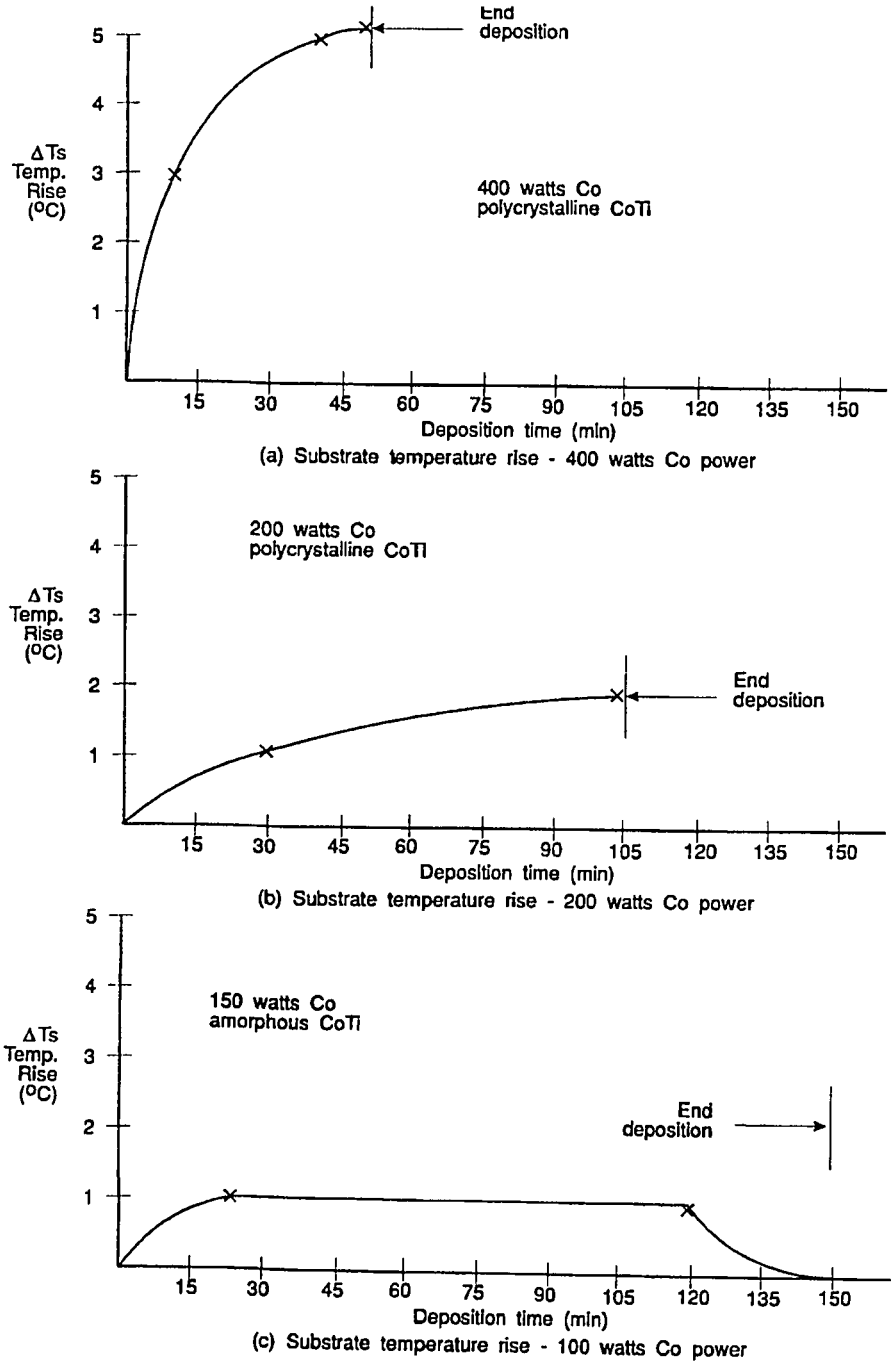

Figure 15. Substrate temperature rise with deposition time

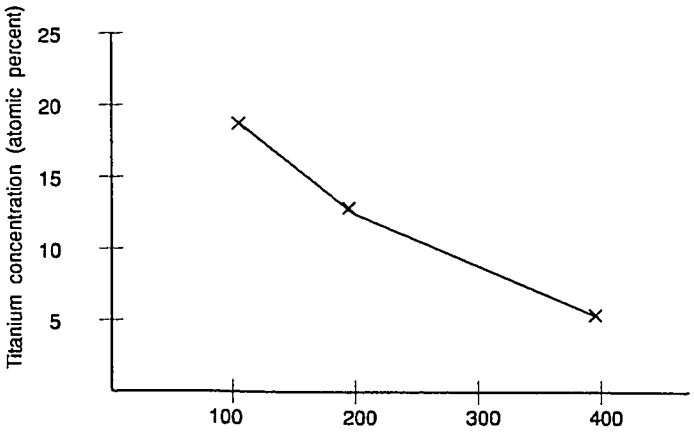

Figure 16. Titanium concentration vs. cobalt sputter power

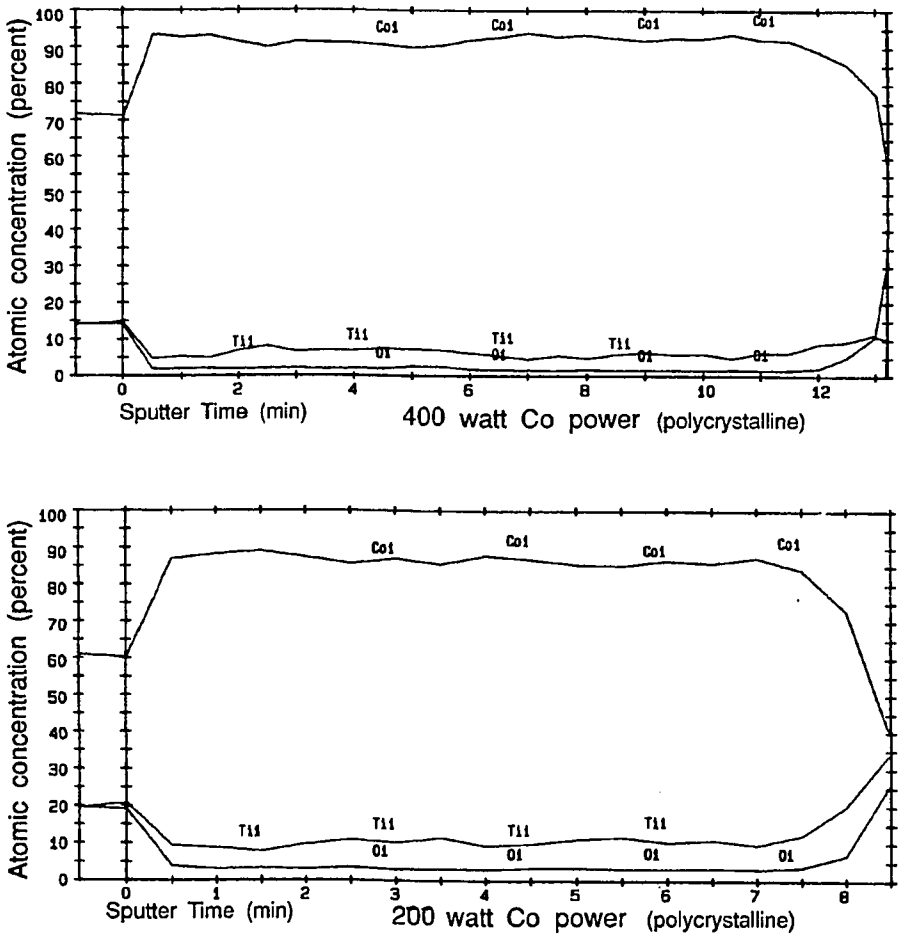

Figure 17. CoTi Auger depth profiles

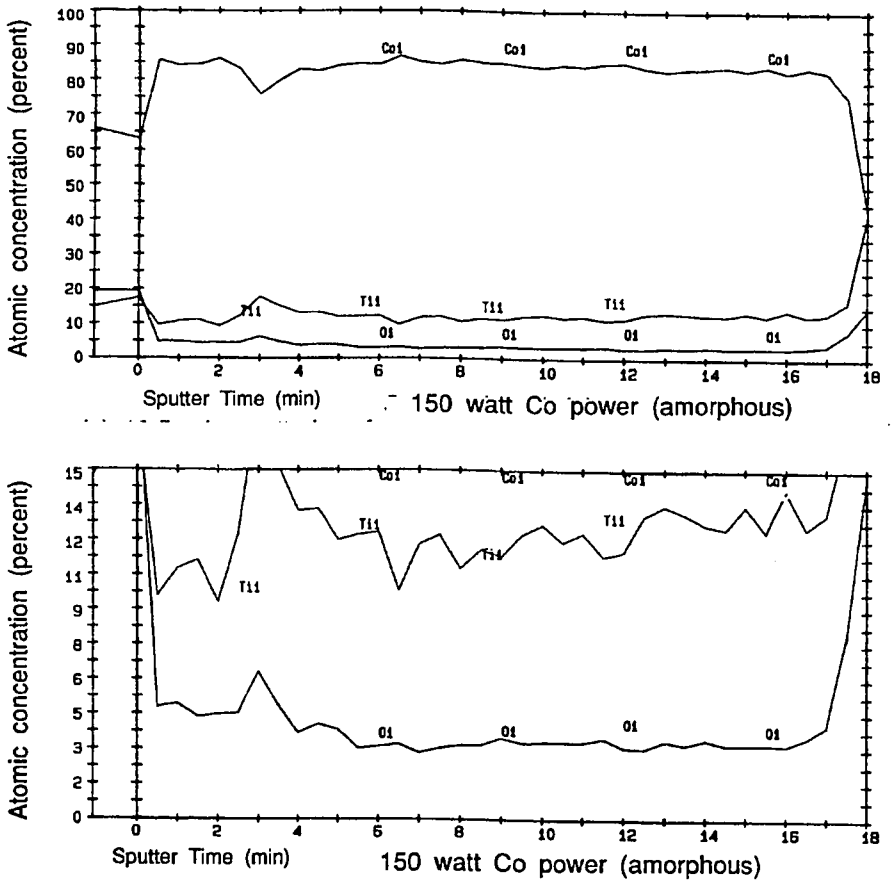

Figure 18. CoTi Auger depth profiles

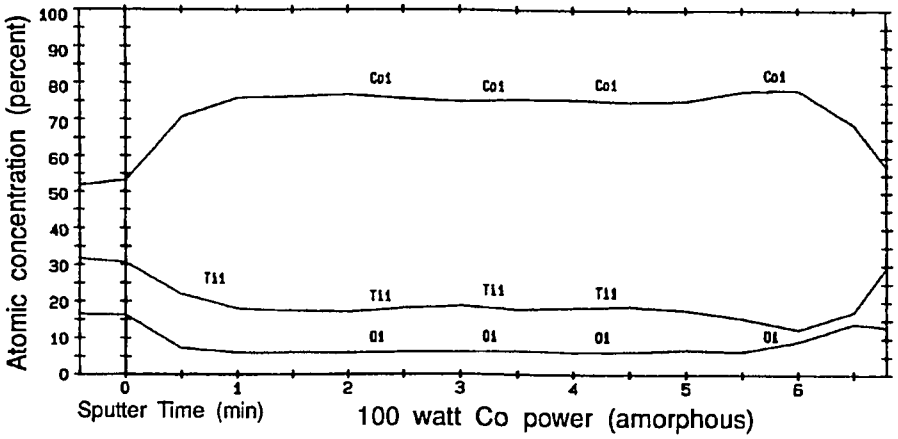

Figure 19. CoTi Auger depth profile

(μohm • cm) vs. cobalt power (watts)$^{-1}$ and R_B vs. atomic percent Ti are shown in Figure 20 and Figure 21, respectively. The graphs showed a discontinuity at approximately 11.5 to 13.5 atomic percent titanium.

The bulk resistivities obtained here for Ti concentration less than 11.5 atomic percent were in the range of 90 to 100 μohm • cm. For Ti concentration greater than 13.5 atomic percent, R_B was approximately 200 μohm • cm.

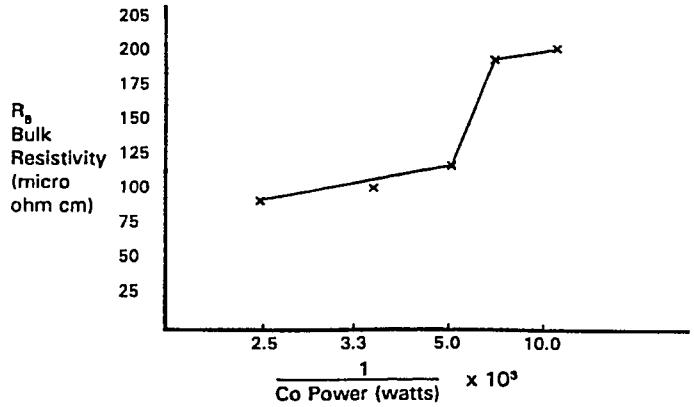

Figure 20. CoTi bulk resistivity vs. cobalt sputter power

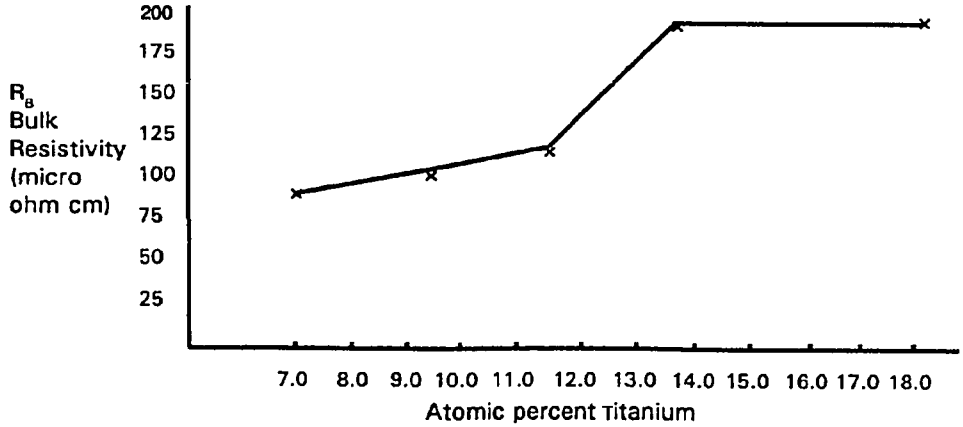

Figure 21. CoTi Bulk resistivity vs. Ti Concentration

Film Structure

Polycrystalline CoTi Structure

A transmission electron diffraction pattern was obtained from a CoTi film sputtered at 200 watts Co power with a Ti concentration of 11.5 atomic percent. The film was sputtered to a thickness of 500 Å onto a carbon grid. The diffraction pattern is shown in Figure 22. The diffraction pattern appeared as a concentric ring pattern with a central broad halo indicating that the structure of the sputtered CoTi film was polycrystalline. The TEM photos of the film surface shown in Figure 23 revealed very small grains in the CoTi film with an average grain size less than 50 Å.

The Transmission Electron Diffraction pattern obtained from a CoTi film sputtered at 400 watt Co power with a Ti concentration of 7 atomic percent is shown in Figure 24a along with a TEM surface photo in Figure 24b. The diffraction pattern also consisted of a concentric ring pattern and the two diffraction patterns together showed that the structures of CoTi films sputtered with the DC Magnetron with Ti concentration between 7 atomic percent to 11.5 atomic percent were polycrystalline. The diffraction patterns from both polycrystalline films were indexed and showed a mixed HCP and Cubic preferred orientation. The films exhibited a highly reflective and opaque surface upon visual inspection. Small voids could be seen in both polycrystalline film structures.

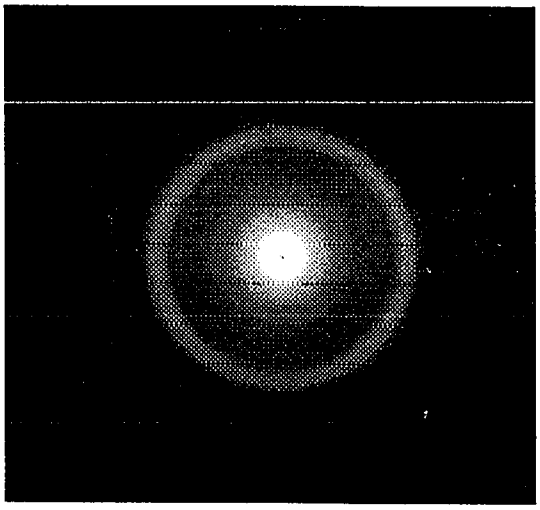

Figure 22. TED diffraction pattern, 200-watt Co power (polycrystalline)

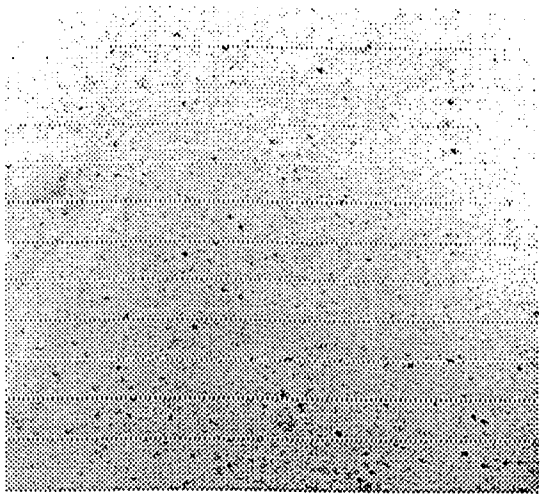

Figure 23. TEM Micrograph, 200 w Co Power (polycrystalline)

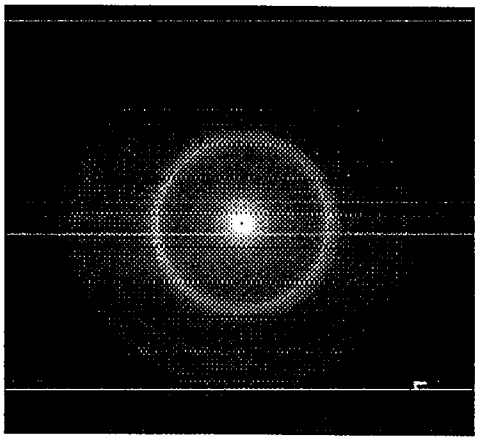

Figure 24(a). TED Diffraction Pattern, 400 w Co power (polycrystalline)

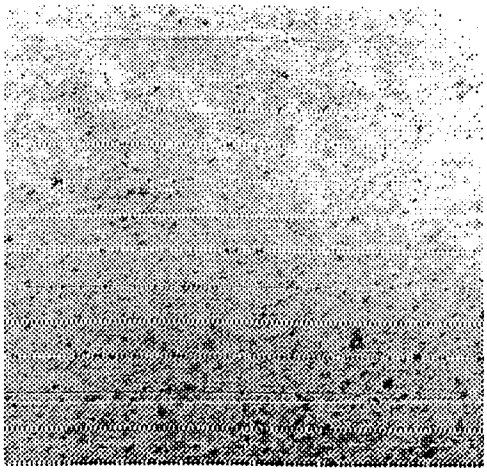

Figure 24(b). TEM Micrograph, 400 w Co Power (polycrystalline)

Amorphous CoTi Structure

An X-ray Diffraction pattern is shown in Figure 25 of a one-micron thick CoTi film sputtered at a Co power of 150 watts with a Ti concentration of 13.5

atomic percent. The pattern exhibited a broad hump or single broad maxima as the X-ray intensity was scanned between 2θ angles of 15.0 degrees and 70.0 degrees using $Cu_{K\alpha}$ radiation. The single broad maxima peak was characteristic of an amorphous film structure. The film was approximately one micron thick and the surface appeared highly reflective and transparent (glassy).

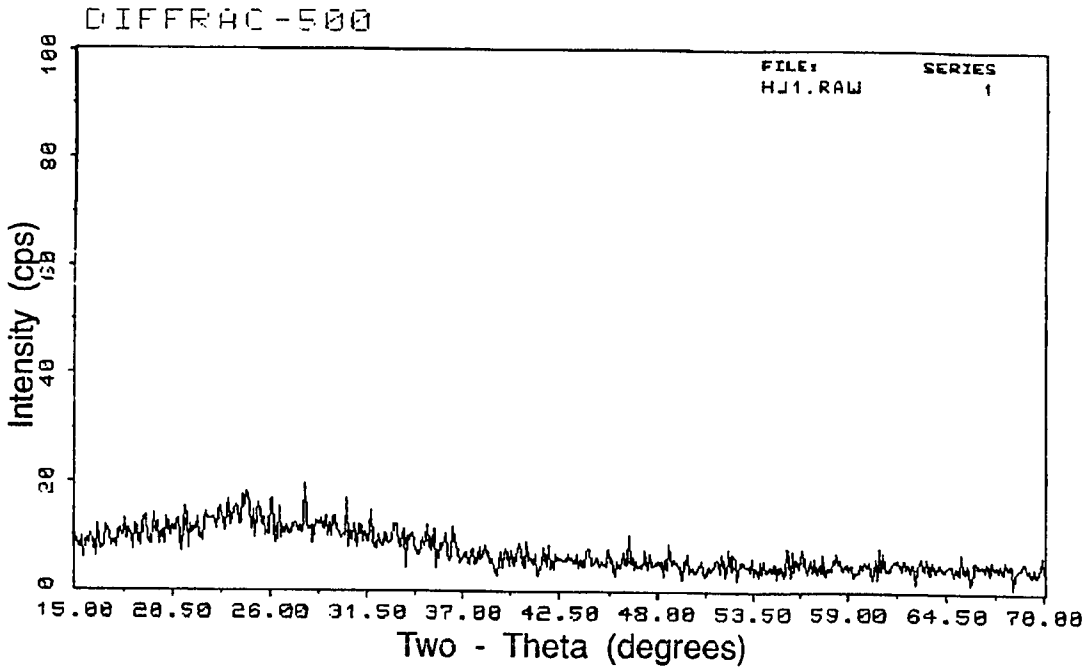

Figure 25. $Co_{86.5}Ti_{13.5}$ X-ray diffraction pattern

Induced Magnetic Anisotropy

Polycrystalline Cobalt-Titanium

Figure 26(a) shows the B-H loop obtained in the direction of the in-plane easy axis which was in the direction of the applied magnetic field, H_{app}, for a 3000 Å polycrystalline $Co_{93}Ti_7$ film deposited at 400 watts Co power and with a Ti concentration of 7 atomic percent. The coercivity, H_c, was 14.5 Oe. Figure 26(b) includes the in-plane B-H traces taken along the easy axis direction and at 90° to the easy axis and showed that the perpendicular direction corresponded to an in-plane hard axis. A magnetic moment (m) vs. H curve was plotted on the Vibrating Sample Magnetometer (VSM) for the $Co_{93}TI_7$ film and is shown in Figure 27. The m vs. H curve showed that the $Co_{93}Ti_7$ alloy was magnetically soft in the direction of the applied field, H_{app}, and was magnetically hard in the ⊥ (out of plane) direction. The small loop in the hard axis curve represented a small residual magnetism in the hard direction.

The in-plane hysteresis loop along the easy axis direction of a polycrystalline $Co_{88.5}Ti_{11.5}$ film deposited at 200-watt Co power is shown in Figure 28a. The in-plane perpendicular trace is shown in Figure 28b. The in-plane easy axis was in the direction of the applied field, H_{app}, and the in-plane ⊥ direction corresponded to a hard axis. The coercivity, H_c, was 7.5 Oe. A magnetic moment (m) vs. H curve was plotted on the VSM for $Co_{88.5}Ti_{11.5}$ and is shown in Figure 29. The m vs. H curve here also showed that the

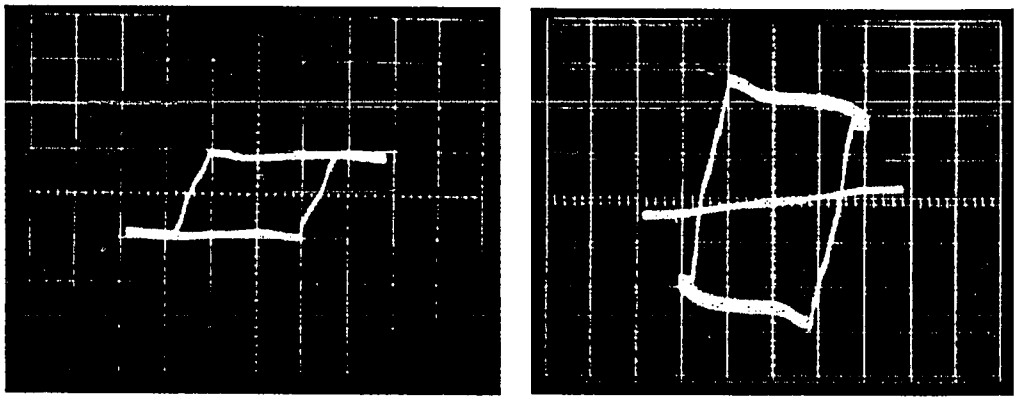

(a) B-H loop in in-plane easy axis direction

(b) B-H loops in the in-plane easy axis and in the in-plane perpendicular directions

Figure 26. $Co_{93}Ti_7$ film (polycrystalline), 400 w Co Power

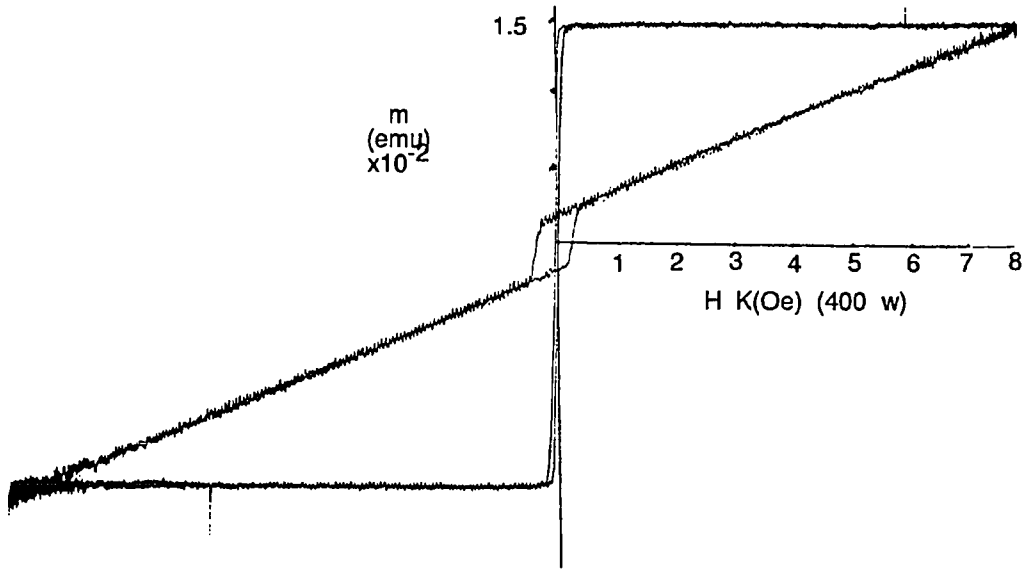

Figure 27. Magnetic moment (m) vs. H curve for polycrystalline $Co_{93}Ti_7$

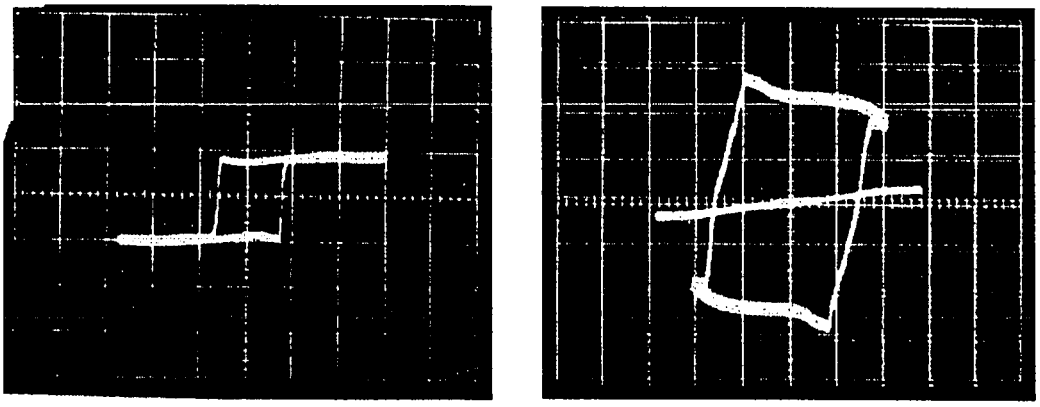

(a) B-H Loop in in-plane easy axis direction

(b) B-H Loops in the in-plane easy axis and in the in-plane perpendicular directions

Figure 28. $Co_{88.5}Ti_{11.5}$ polycrystalline film, 200 w Co power

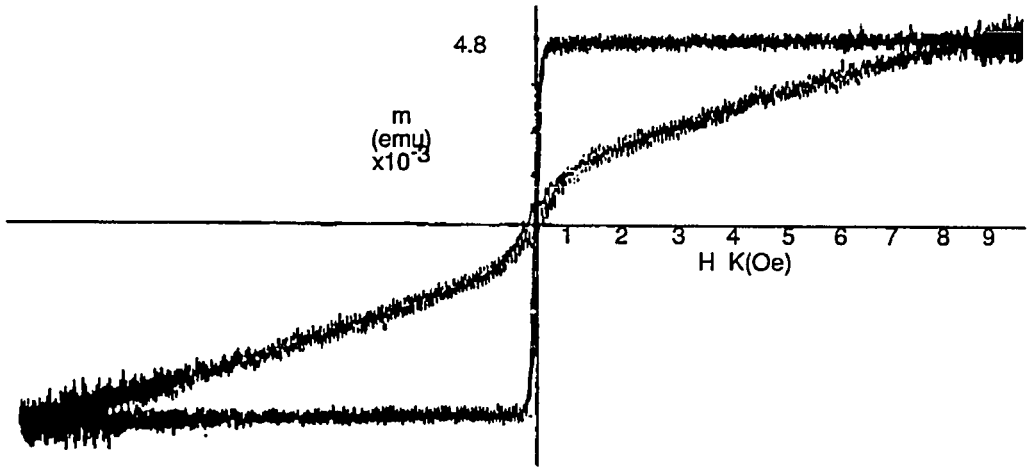

Figure 29. Magnetic moment (m) vs. H curve for polycrystalline $Co_{88.5}Ti_{11.5}$

in-plane easy axis was in the direction of the applied field, H_{app}, and the $\perp$ (out of plane) direction was a hard axis. The dispersion of the easy axis (opening of the loop in the hard axis) was very small for the $Co_{88.5}Ti_{11.5}$ film.

Amorphous Cobalt-Titanium

A B-H loop was obtained from an amorphous $Co_{86.5}Ti_{13.5}$ film sputtered at 150 watts Co power with a titanium concentration of 13.5 atomic percent. The B-H loop showed that an in-plane anisotropy was induced in the direction of the applied field, H_{app} and the in-plane perpendicular direction was a hard axis direction. The coercivity was 14 Oe. This sample shifted in position on the substrate holder and the deposit was slightly non-uniform. The sample was destroyed in handling before an m vs. H curve was obtained.

Cobalt-Titanium Crystallization

A one-micron thick $Co_{86.5}Ti_{13.5}$ film was sputter deposited at 150 watts Co power and is shown in Figure 30. The X-ray diffraction pattern taken from the sample was shown Figure 25. The sample film was amorphous as deposited. However, the Scanning Electron Micrograph of Figure 30 showed that the film was partially delaminated in this specific case due to the necessary omission of the in-situ bake prior to CoTi deposition.

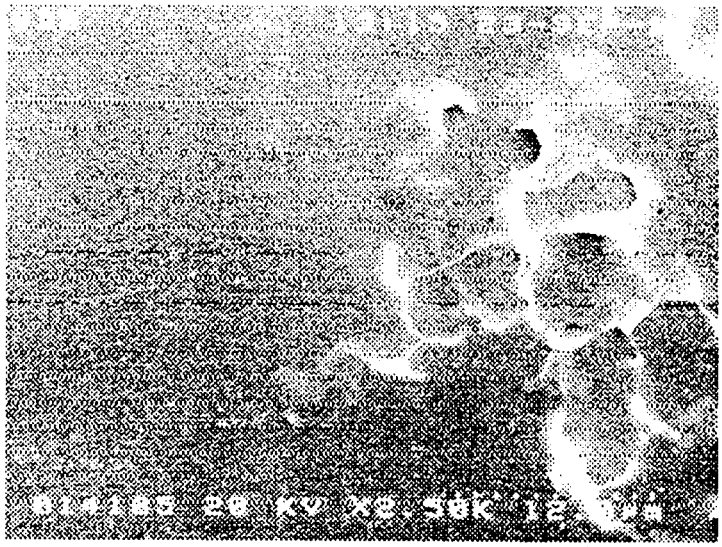

Figure 30. One-micron thick CoTi film $Co_{86.5}Ti_{13.5}$

A Differential Scanning Calorimeter (DSC) scan, shown in Figure 31, was obtained from the amorphous sample and showed a single exotherm which occurred at 470°C or 748°K. This was compared to a DSC Scan from a similar glass slide with no deposited $Co_{86.5}Ti_{13.5}$ which showed no exotherm in the same temperature range.

An X-ray diffraction pattern of the crystallized $Co_{86.5}Ti_{13.5}$ sample was taken using $Cu_{k\alpha}$ radiation and compared to the X-ray diffraction pattern taken prior to thermal cycling in argon. The patterns are shown in Figure 32. The X-ray diffraction pattern and Scanning Electron Micrograph showed that a partial crystallization had occurred in the $Co_{86.5}Ti_{13.5}$ film upon heating in argon. The broad hump still existed in the diffraction pattern and X-ray diffraction peaks from crystalline phases appeared. The crystallization products were identified by XRD as cubic Co_3Ti and cubic $CoTi_2$ phases.

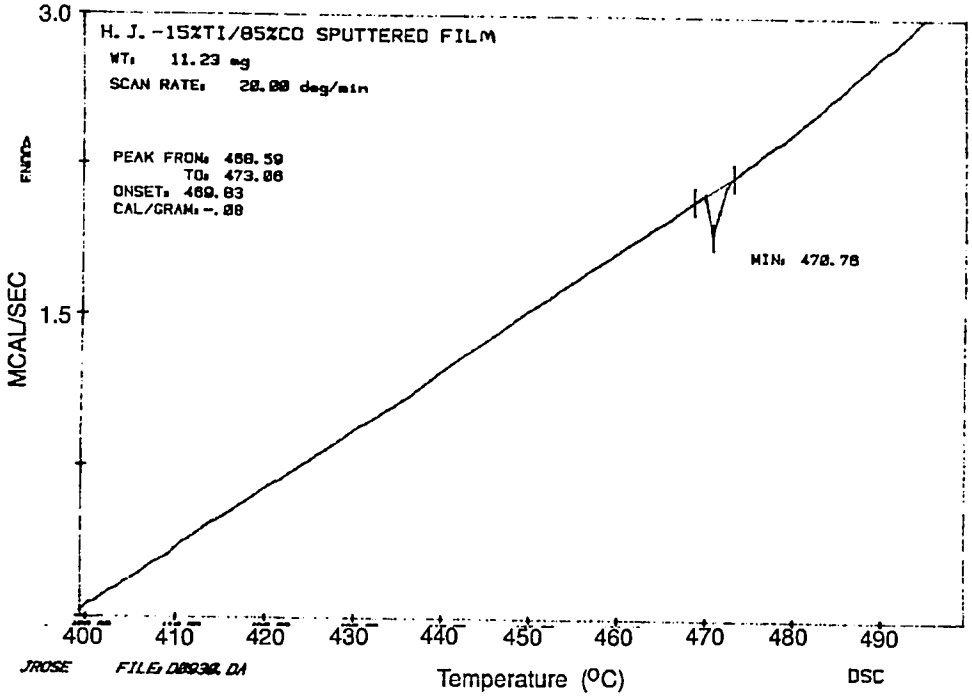

Figure 31. DSC Scan of amorphous $Co_{86.5}Ti_{13.5}$

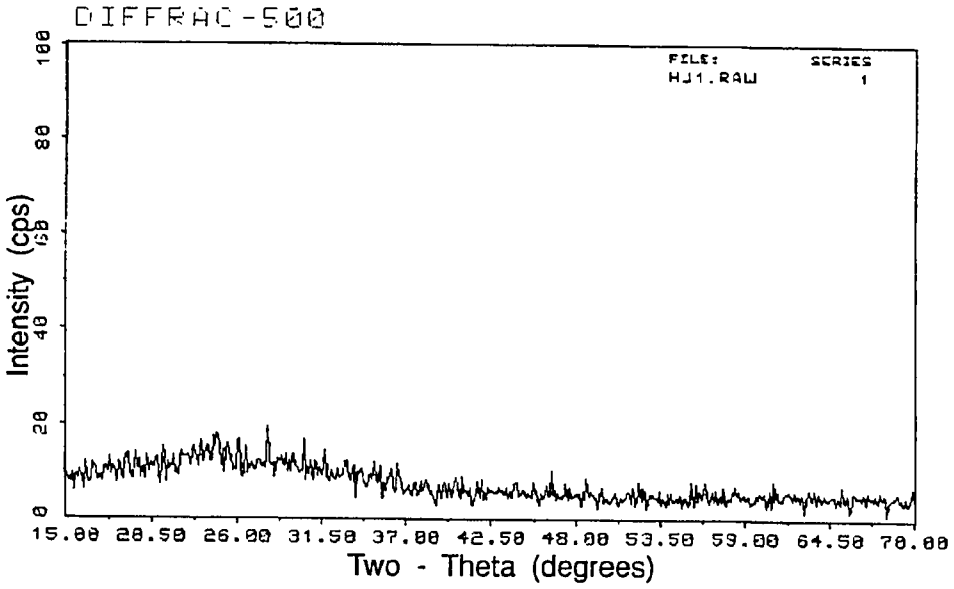

(a) X-ray diffraction pattern prior to thermal cycling

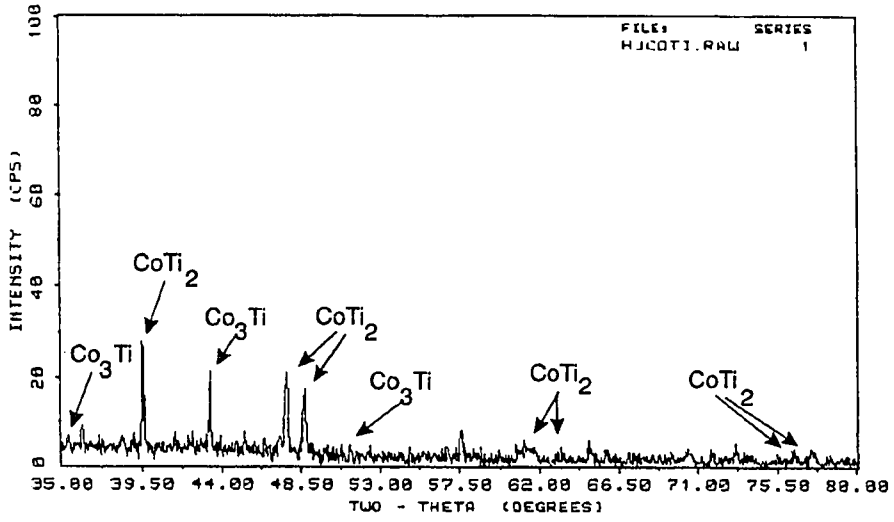

(b) X-ray diffraction pattern after thermal cycling

Figure 32. X-ray diffraction pattern of CoTi

CHAPTER 5

SUMMARY AND DISCUSSION

Summary of Results

Deposition Rate

The deposition rate of cobalt-titanium sputtered alloys using the DC Magnetron configuration and sputtering technique specific to this evaluation increased linearly in proportion to the cobalt deposition power. The deposition rate increased with the arrival rate of the magnetic specie, cobalt, at the substrate surface.

Substrate Temperature Rise

The temperature rise of the substrate during sputter deposition increased with increasing cobalt deposition power. The temperature rise during deposition of polycrystalline CoTi films was measured in the range of 3 to 5 °C and the temperature rise during deposition of amorphous CoTi films was measured in the range of 0 to 1 °C.

Film Composition

The CoTi film composition changed along with the ratio of cobalt power/titanium power. The atomic percent Ti in the CoTi films increased as the Co power was decreased from 400 watts to 100 watts. The Ti concentration

varied from 7 atomic percent to 20 atomic percent in the deposited films. The oxygen concentration in the deposited CoTi films was 5 atomic percent or less.

Bulk Resistivity

The bulk resistivity of the deposited CoTi films increased with increasing titanium concentration. A discontinuity existed in the bulk resistivity vs. atomic percent Ti plot between 11.5 atomic percent Ti and 13.5 atomic percent Ti. The resistivity of polycrystalline CoTi films was in the 90-100 μohm · cm range and the resistivity of the amorphous CoTi films was approximately 200 μohm · cm.

CoTi Film Structure

As the concentration of Ti was increased from 7 atomic percent to 20 atomic percent in the CoTi alloys, a structural transition from a polycrystalline to amorphous structure occurred between Ti concentration of 11.5 to 13.5 atomic percent. For the deposited CoTi films, polycrystalline structures were obtained for Ti less than 11.5 atomic percent and amorphous structures were obtained for Ti greater than 13.5 atomic percent. The average grain size in the polycrystalline films was estimated at grain size less than 50 Å and small voids could be seen in the polycrystalline microstructure. The polycrystalline films showed mixed HCP and Cubic preferred orientation. The polycrystalline CoTi

film surfaces were highly reflective and opaque while the amorphous CoTi film surfaces were highly reflective and semi-transparent (glassy).

Induced Magnetic Anisotropy

Deposition of the CoTi alloy films with the substrate located inside an in-plane applied magnetic field of 1300 Gauss resulted in the formation of induced in-plane magnetic anisotropy in polycrystalline and amorphous films with the in-plane easy axis in the direction of the applied magnetic field. The perpendicular (in-plane and out of plane) directions were directions of hard axis in the polycrystalline and amorphous CoTi films. Small perpendicular (out of plane) anisotropy was obtained in polycrystalline films deposited with Tl concentrations between 7 and 11.5 atomic percent. CoTi magnetic film properties are summarized in Table 1.

Crystallization of CoTi Amorphous Alloys

Upon heating in a pure argon atmosphere at a 20°C/min heating rate, a Differential Scanning Calorimeter scan showed a peak crystallization temperature of 748°K for sputter deposited $Co_{86.5}Ti_{13.5}$ amorphous alloy. The partially crystallized structure consisted of Co_3Ti and $CoTi_2$ intermediate transition phases. The crystallization path consisted of primary crystallization via intermediate phase formation prior to reaching the stable state in the temperature range 298 to 748°K.

Table 1. Summary of Magnetic Film Properties

Film	H_c (Oe)	$H_u = H^h_{Sat}$ (Oe)	$K_u \left(\frac{ergs}{cm^3}\right)$
$Co_{88.5}Ti_{11.5}$ (Polycrystalline)	7	10	1×10^3
$Co_{93}Ti_7$ (Polycrystalline)	14.5	22.5	4.9×10^3

Discussion

Cobalt-Titanium Film Structure

A comparison of results obtained in this investigation using DC Magnetron cosputter was made to previous results reported by G. Suran et al. (references 7,8,9,10,11,12) and J. Aboat et al. (reference 6). A structural transition from a crystalline to an amorphous structure was observed to occur by sputtering at various Ti film concentrations using both RF and DC Magnetron sputtering. The crystalline to amorphous transition occurred at 14 atomic percent Ti and 11.5 to 13.5 atomic percent Ti concentration for RF and DC Magnetron sputtering, respectively. The range of Ti concentration where the crystalline to amorphous transition occurred was similar using both DC and RF sputter techniques. However, when compared to the amorphization range for CoTi alloys reported by Inoue (reference 13), the crystalline to amorphous

transitions for both DC Magnetron and RF sputtered CoTi occurred at a much lower Ti concentration than obtained by Inoue. Furthermore, the amorphization range for CoTi alloys reported by Inoue covered a narrow Ti concentration range of approximately 1 to 3 atomic percent which was centered around the cobalt-titanium eutectic composition of 22 atomic percent Ti. These differences could be explained by the fact that typical quenching rates for vapor quenching techniques such as sputtering (10^{13}°K/sec.) are several orders of magnitude greater than the typical arc-melted liquid quenching rate (10^{6}°K/sec.) employed by Inoue.

The faster quench rates for vapor-quenching techniques generally extend the amorphization range beyond that obtained by the slower liquid-quenching techniques. When compared to previous results from Inoue, the compositional dependence of the crystalline to amorphous transition and the width of the amorphization concentration range for CoTi alloys appears to be strongly influenced by the magnitude of the quenching rate of the rapid solidification process employed for amorphization.

The microstructure of polycrystalline films deposited using DC Magnetron and previously reported RF sputtering both contained grains of similar size which were less than 50 angstroms. Transmission Electron Diffraction patterns of polycrstalline films showed mixed HCP and Cubic preferred orientation (texture) in DC Magnetron and RF sputtered films. However, Transmission

Electron Micrographs of DC Magnetron sputtered-polycrystalline CoTi films revealed small voids in the film structure and the films were more porous than films reported using RF sputtering. The higher bulk resistivities, R_B, obtained for DC Magnetron sputtered CoTi films were attributed to microvoids in the film structure.

The presence of voids in the DC Magnetron sputtered CoTi films can possibly be explained by the fact that the sputtering was performed at very low deposition rates (10 to 20 angstroms per minute for amorphous CoTi) and the titanium was deposited at a small oblique angle which causes a shadowing effect in the deposited film and enhances void formation. This was in contrast to previously reported RF sputtered amorphous CoTi films which were deposited at 40 angstroms per minute deposition rate and the Co and Ti species were deposited from a single target with perpendicular arrangement with respect to the substrate location.

Cobalt-Titanium Magnetic Properties

Values of the in-plane induced anisotropy constants, $K_u(10^3$ ergs/cm$^3)$ for DC cosputtered-polycrystalline CoTi films in this investigation were approximately one order of magnitude less than the anisotropy constants previously reported using RF sputtering (10^4 ergs/cm^3). This could be attributed to the presence of microvoids observed in the microstructures of the

cosputtered CoTi films. This is consistent with the directional order and Globus models of ferromagnetism in polycrystalline materials. The magnetic interaction between the magnetic atoms which is responsible for ferromagnetism and magnetic anisotropy in the material is strongly dependent upon close proximity of pair atoms and grains aligned with preferrential orientation in the presence of an applied magnetic field by these models. Voids in the cosputtered CoTi film microstructure reduce the magnetic coupling between grains and the strength of the induced magnetic anisotropy, represented by K_u, was reduced.

The magnetic coercivities, H_C, obtained for polycrystalline CoTi films in this investigation ranged from 7 to 14.5 Oe. These coercivities were equivalent to values of coercivites reported by G. Suran (references 7 through 12) using RF sputtering. However, J.A. Thompson et al. (reference 3) obtained coercivity, H_C, between 1 to 3 Oe in deposited CoTi films with oxygen concentrations of 2 atomic percent or less in the film The coercivity was reported by Thompson to increase with higher oxygen concentration above 2 atomic percent. At higher oxygen concentrations, Ti segregates from solution in the bulk film and reacts with oxygen to form titanium oxide. Narrower hysteresis loops with reduced coercivities, H_C, are possibly obtainable using RF or DC Magnetron sputtering of CoTi films with maximum oxygen concentration of 2 atomic percent.

Substrate Temperature

Substrate temperature was measured in this investigation of DC Magnetron sputtered CoTi using a chromel-alumel thermocouple mounted close to the substrate. Previous RF investigations reported substrate temperature measurements using thin film thermocouples. For extended deposition times which were greater than 60 minutes, substrate temperatures for RF depositions were reported to increase up to 100°C. The deposited films reportedly consisted of a three-layer structure consisting of a bottom layer close to the substrate, a top layer at the film-air interface and an intermediate transition layer situated between them. It was reported that the initially deposited layer close to the substrate primarily contained in-plane anisotropy, K_u, while the top layer contained large perpendicular (out of plane) anisotropy, K_p. The occurrence of K_p was attributed to gradual increase in substrate temperature during RF sputter deposition. The corresponding B-H loops showed the presence of a multi-layered structure.

Using the DC Magnetron sputtering at large target to substrate spacing, films were deposited for times up to 150 minutes with measured substrate temperature rise less than 5°C. The corresponding B-H loops did not indicate a multi-layered structure as shown by the B-H curves obtained in this investigation. The comparison between the DC Magnetron and RF sputter deposition of CoTi indicated that significantly less substrate heating occurred

during the DC Magnetron sputtering employed in this thesis investigation when compared to results reported from previous RF sputtered CoTi investigations.

Cobalt-Titanium Crystallization

The crystallization path upon heating of amorphous $Co_{86.5}Ti_{13.5}$ deposited by DC Magnetron cosputter proceeded by initial crystallization of intermediate $CoTi_2$ and Co_3Ti phases at 748°K peak temperature via primary crystallization. Crystallization of arc-melted $Co_{78}Ti_{22}$ amorphous alloy of eutectic composition reported by Inoue proceeded by initial crystallization of metastable Co_2Ti at 777°C. The sputtered $Co_{86.5}Ti_{13.5}$ and liquid-quenched $Co_{78}Ti_{22}$ both appeared to crystallize initially by primary crystallization of intermediate cobalt-titanium phases. However, the initial crystallization of sputtered and arc-melted cobalt-titanium occurred at distinctly different temperatures (748°K and 777°K). The initial crystallization product for sputtered $Co_{86.5}Ti_{13.5}$ consisted of intermediate $CoTi_2$ and Co_3Ti phases while the initial crystallization of arc-melted $Co_{78}Ti_{22}$ consisted of metastable Co_2Ti.

Primary crystallization requires long-range diffusion. It is highly possible that the activation energy for diffusion in the sputtered $Co_{86.5}Ti_{13.5}$ amorphous film was different from the activation energy for arc-melted $Co_{78}Ti_{22}$ due to the influence of differences in alloy composition and effective quench rates used during solidification of the alloys. Consequently, the

crystallization upon heating in pure argon of cosputtered amorphous $Co_{86.5}Ti_{13.5}$ appeared to proceed to the final stable state via a crystallization path which was different from the reported crystallization path of amorphous $Co_{78}Ti_{22}$ prepared by arc-melting.

CHAPTER 6

CONCLUSIONS

Using the DC Magnetron Box Sputter System and large target-to-substrate distance (15 inches), polycrystalline and amorphous cobalt-titanium films were produced by cosputter deposition. The polycrystalline and amorphous structures were obtained during sputter depositions where the measured substrate temperature rise, ΔT_S, was 5°C maximum. The measured substrate temperature, T_S, was maintained in the temperature range where T_S/T_M was less than 0.1, where T_M was the equilibrium melting temperature of the deposited CoTi film. The maximum substrate temperature obtained by DC cosputter represented an improvement over that reported for RF sputtering. The polycrystalline and amorphous structures resulted from the low mobilities of deposited Co and Ti species on an amorphous glass substrate during heterogeneous nucleation and growth from the vapor state. The low surface mobilities were due to high surface diffusion activation energies for Co and Ti at low substrate temperature. For Ti concentration less than 11.5 atomic percent, the CoTi structure was polycrystalline. For Ti concentration greater than 13.5 atomic percent, the CoTi structure was amorphous. When compared to previous results, the compositional dependence of the crystalline to amorphous transition appeared to be more related to the quenching rate upon

solidification than to the differences between RF and DC sputtering techniques. Higher bulk resistivities, R_B, obtained in DC Magnetron sputtered CoTi films were attributed to the presence of microvoids in the film microstructure.

When cosputtered in the presence of an applied in-plane static magnetic field of 1300 Gauss, in-plane magnetic anisotropy was induced into both polycrystalline and amorphous CoTi films with anisotropy constant, K_u, between 1×10^3 to 4.9×10^3 ergs/ cm^3. Coercivity, H_u, was between 7.0 to 14.5 Oe. The induced magnetic anisotropy was in the direction of the applied magnetic field. For polycrystalline CoTi, the in-plane anisotropy resulted from magnetically induced-preferential orientation of grains with mixed HCP and Cubic texture.

Upon heating a cosputtered amorphous $Co_{86.5}Ti_{13.5}$ film in pure argon ambient, a peak crystallization temperature, T_X, was observed at 748°K. The crystallized product consisted of intermediate $CoTi_2$ and Co_3Ti transition phases in an amorphous matrix. The crystallization path began by primary crystallization of intermediate cobalt-titanium phases.

A recommended follow-up to this investigation would include repeat experimentation using DC Magnetron sputter at large target-to-substrate distance in an applied in-plane magnetic field, using a single cobalt-titanium target with no oblique sputter component. Repeated experimentation at higher deposition rates is also recommended. Extensive measures such as in-situ

baking of the deposition chamber and vacuum pumping the chamber to the low (2×10^{-7} Torr) vacuum range prior to sputter deposition should be employed to reduce the oxygen concentration in the CoTi to a maximum of 2 atomic percent. These techniques could reduce the number of voids in the sputtered CoTi microstructure and possibly result in narrower in-plane hysteresis loops with smaller H_C in the film easy axis direction. These techniques could result in larger values of induced magnetic anisotropy constant, K_u, than obtained in this investigation.

Further recommendations would include investigation of the crystallization path upon heating of sputter deposited-amorphous cobalt-titanium films at higher temperatures than employed in this investigation to determine the crystallization path followed by the amorphous films to the final stable state. A follow-up to this investigation should also include determination of the enthalpy of crystallization, ΔH_{crys}, and the activation energy, E_a, associated with the crystallization of CoTi films.

REFERENCES

1. F.E. Luborsky, Amorphous Metallic Alloys, Edited by F.E. Luborsky, Butterworth & Company, Publishers, 1983 (1).

2. When Shan Chan, Katsuya Mitsuoka, Hideki Miyajima and Soshin Chikazumi, Effect of Ti-Impurities on Ferromagnetic Properties of Fe, Co, Ni, Journal of the Physical Society of Japan, Vol 48, No. 3, March 1980 (822).

3. J. A. Thompson and D.A. Stevenson, The Effects of Oxygen on Cobalt-Titanium and cobalt-Platinum Thin Films, IEEE Trans. on Magnetics, Vol. MAG-22, No. 5, September 1986 (635).

4. G. Suran and P.Gerard, The Effect of Rare Gas Implantation on the Magnetic Properties of Amorphous CoTi Thin Films, IEEE Trans. on Magnetics, Vol. MAG-23, No. 5, Septemeber 1987 (2740).

5. Y. Maehata, S. Tsunashima and S. Uchiyama, Induced Anisotropy of Co-Zr and Co-Ti Amorphous Films, IEEE Trans. on Magnetics, Vol. MAG-22, No. 5, September 1986 (1107).

6. J. A. Aboaf and E. Klokholm, Amorphous Magnetic Alloys of Cobalt-Titanium, J. Appl. Phys. 52 (3), March 1981 (1844).

7. G. Suran, J. Sztern, J.A. Aboaf and T.R. McGuire, Magnetic Properties of Amorphous Ferromagnetic $Co_{100-x}Ti_x$ Thin Films, IEEE Trans On Magnetics, Vol. MAG - 17, No. 6, November 1981 (3065).

8. G. Suran, K. Ounadjela and F. Machizavd, Magnetic Properties of Amorphous Co-Ti Thin Films With a Perpendicular and In-Plane Uniaxial Anisotropy, J. Appl. Phys. 61 (8), 3658, April 1987.

9. G. Suran, K. Ounadjela, J. Sztern and C. Sella, Field Induced Anisotropy in Amorphous $Co_{100-x}Ti_x$ Thin Films, J. Appl. Phys. 55(6), 1757 March 1984.

10. G. Suran, K. Ounadjela and F. Machizard, Evidence for Structure-Related Induced Anisotropy in Amorphous CoTi Soft Ferromagnetic Thin Films, Phys. Rev. Lett., Vol. 57, No. 24, 3109 December 1986.

11. R. Zuberek, H. Szymczak, G. Suran and K. Ounadjela, Investigations of Magnetostriction in $Co_{86}Ti_{14}$ Amorphous Thin Films, Thin Sol. Films, 188, No. 1, (1) July 1990.

12. G. Suran and K. Ounadjela, Magnetically Induced Anisotropy in Amorphous $Co_{1-x}Ti_x$ Thin Films Studied by Various Techniques, J. Magn. Magn. Mat., 54-57 (1986) 237-238.

13. A. Inoue, K. Kobayashi, C. Suryanarayana and T. Masumoto, An Amorphous Phase in Co-Rich CoTi Alloys, Scripta Metallurgica, Vol. 14, (119) 1980.

14. Ibid.

15. Ibid.

16. D.A. Porter and K.E. Easterling, Phase Transformations in Metals and Alloys, Van Nostrand-Reinhold, 1981 (3).

17. D.R. Gaskell, Introduction to Metallurgical Thermodynamics, McGraw-Hill Col, 1981 (156).

18. R.E. Reed-Hill, Physical Metallurgy Principles, Second Edition, PWS-Kent Publ, 1973 (502).

19. D.R. Uhlmann and H. Yannon in The Formation of Glasses, Glass Science and Technology, Vol. 1, Edited by D.R. Uhlmann and N.J. Kriedl, Academic Press, 1983 (8).

20. H.A. Davies, in The Formation of Metallic Glasses, Physics and Chemistry of Glasses, Vol. 17, No. 5, October, 1976 (159).

21. P.F. James, Nucleation in Glass Forming Systems, Nucleation and Crystallization in Glasses, Edited by J.H. Simmons, D.R. Uhlmann and G.H. Beall, American Ceramic Society, 1982 (1).

22. J.P. Hirth in Vapor Deposition, Edited by C.F. Powell, J.H. Oxley and J.M. Blocher, Jr., John Wiley and sons, 1966 (126).

23. J.P. Hirth and G.M. Pound in Condensation and Evaporation, Edited by Bruce Chalmers, Progress in Materials Science, Vol. 11, MacMillan Co., 1963 (15).

24. J.W. Christian, The Theory of Transformations in Metals and Alloys, Second Edition, Part I, Pergamon Press, 1975 (418).

25. B. Lewis and J.C. Anderson, Nucleation and Growth of Thin Films, Academic Press, 1978 (103).

26. M.G. Scott and R. Maddin, Comparisom Between Vapor and Liquid-Quenched Amorphous Alloys, Second Int. Conf. on Rapidly Quenched Metals, Edited by N.J. Grant and B.C. Giessen, Vol. 1, 1975 (249).

27. A.R. Adamson, Physical Chemistry of Surfaces, 5th Ed., John Wiley and Sons, 1990 (364).

28. O.F. Devereux, Topics in Metallurgical Thermodynamics, Krieger Publisher, 1989 (429).

29. Ref. 22, p. 127.

30. Ref. 28, p. 436.

31. Ibid.

32. W.D. Kingery, H.K. Bowen and D.R. Uhlmann, Introduction to Ceramics, Second Edition, John Wiley & Sons, 1976 (328).

33. K.H. Behrndt, Phase and Order Transitions During and After Film Deposition, Journal Appl. Physics, Vol. 10, Sept. 1966 (3841).

34. Ref. 23, p. 45.

35. C.A. Neugebauer, Condensation, Nucleation and Growth of Thin Films, Handbook of Thin Film Technology, edited by L. Maissel and R. Glang, McGraw-Hill, 1970 (8-10).

36. Carl V. Thompson and Frans Spaepen, On the Approximation of the Free Energy Change on Crystallization, Acta Metallurgica, Vol. 27, 1979 (1855).

37. A.E. Owen in The Glass Transition, Amorphous Solids and the Liquid State, Edited by N.H. March, R.A. Street and M. Tosi, Plenum Press, 1985 (405).

38. N. Saunders and A.P. Miodownick, Thermodynamic Aspects of Amorphous Phase Formation, J. Mater. Res. 1 (1), January 1986 (38).

39. Ref. 1, p. 12.

40. I. Gutzow and I. Avramov, On the Mechanism of Formation of Amorphous Condensates from the Vapor Phase, J. Non-Crystalline Solids, 16 (1974) 128.

41. Ref. 24, p. 420.

42. I. Gutzow, D. Kashciev and I. Avramov, in Nucleation and Crystallization in Glass Forming Melts, J. Non-Crystalline Solids, 73 (1985) 477.

43. J.W. Mullin, Crystallisation, CRC Press, Butterworth & Co., 1972 (174).

44. C.G. Bergeren in General Aspects of the Crystallization of Glass, Introduction to Glass Science, Plenum Press, 1972 (173).

45. R. Elliott, Eutectic Solidification Processing, Butterworths, 1983 (37).

46. M.G. Scott in Crystallization; Amorphous Metallic Alloys, Edited by F.E. Luborsky, Butterworths, 1983 (144).

47. U. Köster and U. Herold, Topics in Applied Physics, Vol. 46, Glassy Metals I, Edited by H.H. Güntherodt and H. Beck, Springer-Verlag, 1981 (225).

48. Ibid.

49. Ref. 46, p. 156.

50. Ref. 46, p. 157.

51. Ref. 47, p. 234.

52. B.D. Cullity, Introduction to Magnetic Materials, Addison-Wesley Publishing Co., 1972 (233).

53. Ibid.

54. Ibid.

55. S. Chikazumi, Physics of Magnetism, Krieger Publ. Co., 1964 (138).

56. Ref. 52, p. 234.

57. Ref. 52, p. 237.

58. M.A. Escobar and R. Valenzuela, Analytical Prediction of the Magnetization Curve and the Ferromagnetic Hysteresis Loop, Journal of Appl. Phys., 54(10), Oct. 1983 (5935).

59. M. Le Floc'h, Analytical Expression of the First Magnetization Curve in Soft Magnetic Polycrystalline Materials, Journal of Appl. Phys., 67(1), Jan. 1990 (405).

60. Y. Ishii and M. Sato, Magnetic Behaviours of Two Spheres Which Contact Each Other With an Area, J. Appl. Phys. 57(2), 15 Jan. 1985 (465).

61. Y. Ishii and M. Sato, Magnetic Behaviours of Elongated Single-Domain Particles by the Chain of Spheres Model, J. Appl. Phys. 59(3), 1 Feb. 1986 (880).

62. H. Fujimori, Magnetic Anisotropy, Amorphous Metallic Alloys, edited by F.E. Luborsky, Butterworths, 1983 (308).

63. E.P. Wohlfarth, Itinerant Electron Model of Magnetic Properties, Amorphous Metallic Alloys, edited by F.E. Luborsky, Butterworths, 1983 (296).

64. Ref. 62, p. 310.

65. J.C. Slonczewski, Magnetism, Edited by G. Rado, Academic Press, 1963 (205).

66. J.W. Edington, Practical Electron Microscopy In Materials Science, Van Nostrand Reinhold Co., 1976 (44).

APPENDIX

1. Glass Substrates

The glass substrates used for the experiments were 3/4 x 3/4 x 0.010 inch in dimension. An Energy Dispersive X-ray spectrum of the glass slide plus 500 Å CoTi film is shown in Figure 33. The major elements of the glass material consisted of Si, K and oxygen with a small amount of Zn.

2. Permanent Magnets

The permanent magnets were used to establish the in-plane magnetic field, H_{app} = 1300 Gauss. An Edax spectrum of a representative sample of permanent magnet material is shown in Figure 34. The elemental constituents of the permanent magnet material consisted of Sm, Co and Fe and the magnets were cobalt-rich SmCoFe.

3. Plain Carbon Steel

The U-shaped return path for magnetic flux in the permanent magnet assembly was established by utilizing a sheet of plain carbon steel which was bent into the U-shape. Microscopic inspection of the polished surface showed small inclusions in the Fe-C matrix. The overall composition was estimated by Edax to consist of 1.25 weight percent Mn, 98 weight percent Fe and C < 1.0

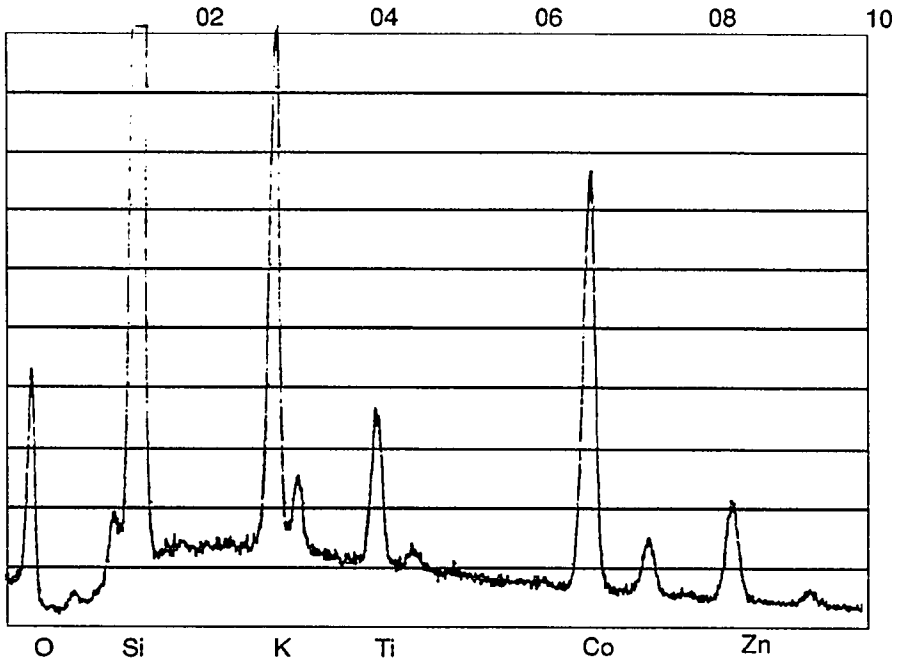

Figure 33. X-ray spectrum of glass slide plus CoTi film

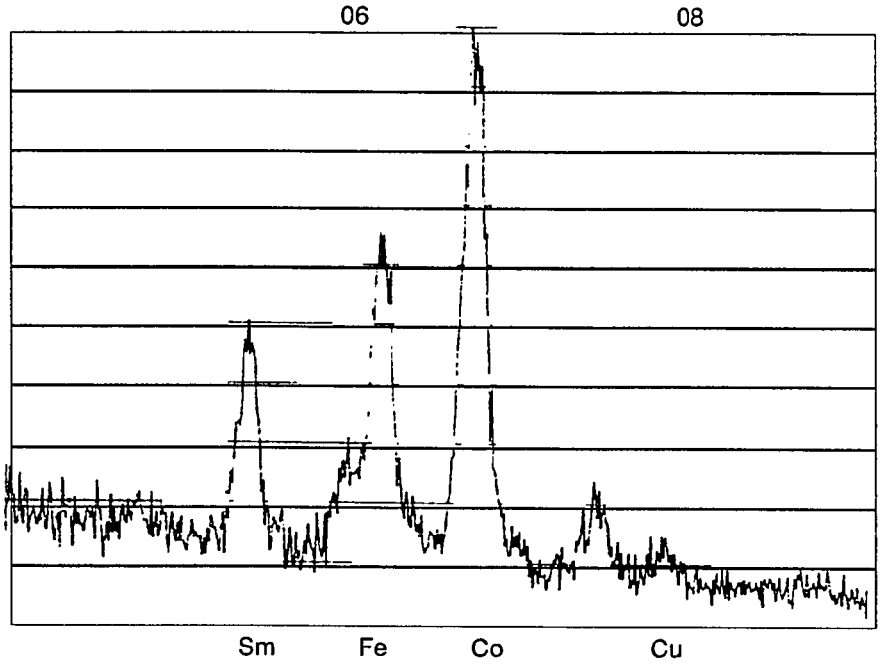

Figure 34. Edax spectrum of permanent magnets

weight percent. An Edax spectrum of the plain carbon steel is shown in Figure 35. A reduced-raster Edax spectrum of the small inclusions is shown in Figure 36 and showed that the inclusions were Mn-rich.

4. Indexing Transmission Electron Diffraction Patterns

The Transmission Electron Diffraction patterns were indexed using the procedure outlined by Edington[66].

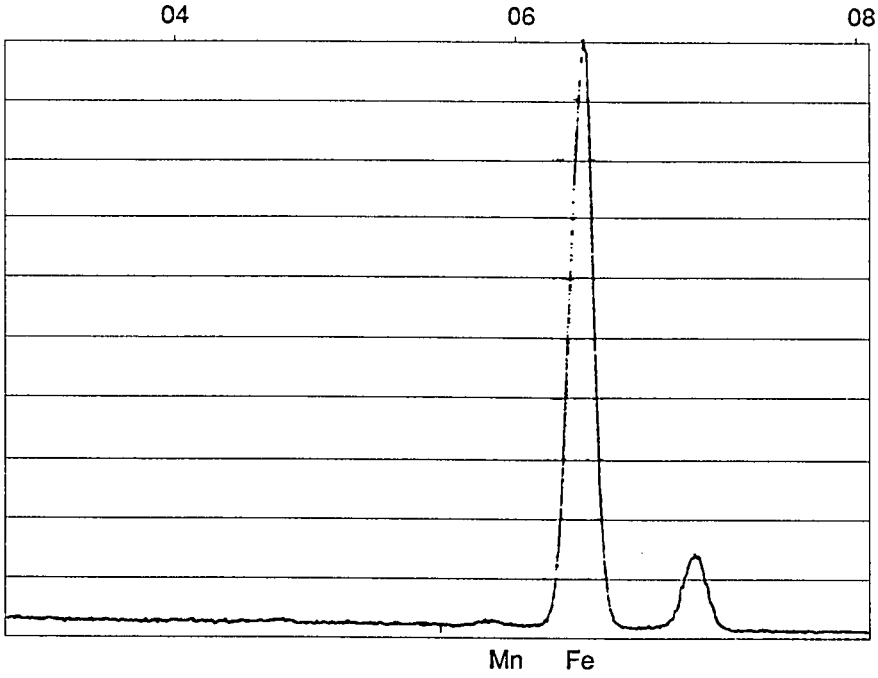

Figure 35. X-ray spectrum of plain carbon steel

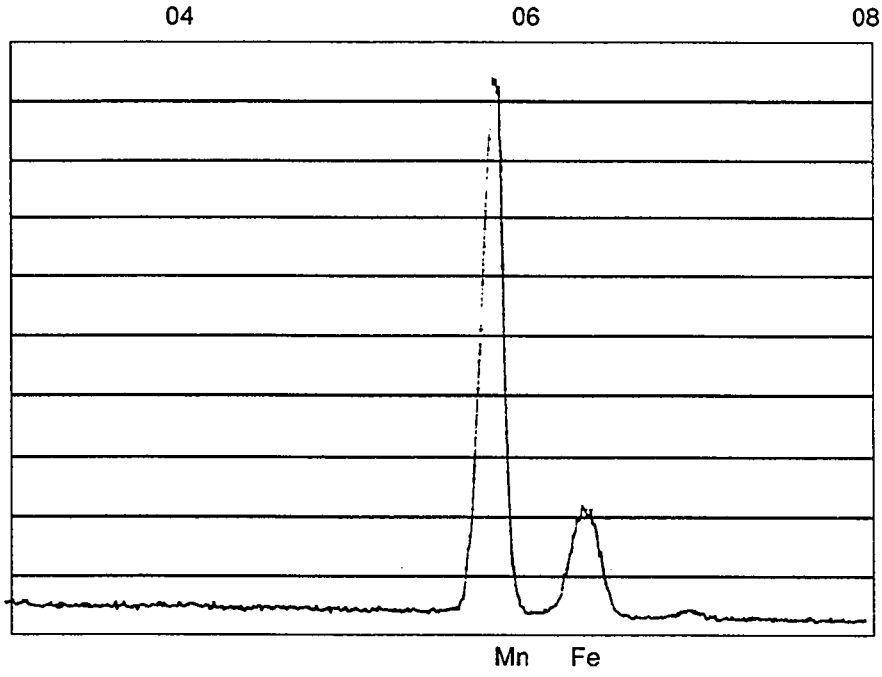

Figure 36. X-ray spectrum of Mn-rich inclusions in plain carbon steel